Journal of Optics

PAPER • **OPEN ACCESS**

Photoconductive emitters for pulsed terahertz generation

To cite this article: David R Bacon *et al* 2021 *J. Opt.* **23** 064001

View the article online for updates and enhancements.



IOP ebooks™

Bringing together innovative digital publishing with leading authors from the global scientific community.

Start exploring the collection–download the first chapter of every title for free.

This content was downloaded from IP address 203.181.243.17 on 20/05/2021 at 09:00

OPEN ACCESS
IOP Publishing
Journal of Optics
J. Opt. **23** (2021) 064001 (29pp)
https://doi.org/10.1088/2040-8986/abf6ba

Photoconductive emitters for pulsed terahertz generation

David R Bacon*, Julien Madéo and Keshav M Dani

Femtosecond Spectroscopy Unit, Okinawa Institute of Science and Technology Graduate University, 1919-1 Tancha, Onna-son, Kunigami, Okinawa 904-495, Japan

E-mail: David.Bacon@oist.jp

Received 25 December 2020, revised 18 March 2021
Accepted for publication 9 April 2021
Published 27 April 2021



Abstract

Conceived over 30 years ago, photoconductive (PC) emitters have proved essential in the development and spread of terahertz technology. Since then, not only have they been used extensively in a wide range of spectroscopic and imaging applications, they have also undergone significant improvements in performance, leading to their use for broadband or non-linear spectroscopy. In this review article, we provide an overview of the literature, highlighting the key milestones in the progression of the PC emitter. We also investigate the future of PC technology and review the existing challenges.

Keywords: terahertz, photoconductive, antenna

(Some figures may appear in colour only in the online journal)

1. Introduction

The development and application of terahertz (THz) technology has seen significant progress over the past 30 years. This has been driven, in-part by the development of photoconductive antennas (PCAs) [1–3], in parallel with THz time-domain spectroscopy (TDS) [4, 5]. Since its first demonstration in 1990, photoconductive (PC) emission and detection of THz radiation has been widely studied, leading to the application of THz radiation in various areas including non-destructive imaging and spectroscopy of pharmaceuticals [6, 7], spectral fingerprint analysis of drugs-of-abuse and explosives for security scans [8, 9], and the biomedical dental imaging and identification of cancerous skin tissue [10–12]. The unique ability of the THz radiation to excite intermolecular vibrations has provided the capability to study large biomolecules, giving rise to various areas of biomedical research with the use of THz-TDS [13–15]. Furthermore, the addition of an optical excitation to perform optical-pump-THz-probe spectroscopy has allowed the study of the conductivity and time-resolved photocarriers dynamics in various semiconductors [16, 17], as well as defect detection in the semiconductor industry [18].

Recent developments in ultrafast amplified laser systems have brought about the generation of significantly higher THz fields, compared with those achievable using a standard oscillator laser. This has led to a new area of investigation, studying the non-linear characteristics of materials in condensed matter physics [19, 20]. Among many others, these include investigations into carrier transport in semiconductor and superconductors, and the ionization of Rydberg states in Na atoms [21, 22]. Furthermore, it has been shown that intense THz radiation can be used to control and manipulate electronic, spin and ionic properties of molecules and solids [23]. However, many of these studies have utilised accelerator-based synchrotron facilities [24] or other established table-top methods of THz generation, such as non-linear optical crystals [25–27] and two-colour air plasma [28–30]. While PC emission is highly successful and widely used in the low-field regime, it is under-utilised at high-fields owing mainly to saturation effects. This is despite several desirable properties which include THz output fields greater than 100 kV cm^{-1} [31, 32], simple system alignment, bias-controllable output field and electrically switchable polarisation [33]. Further research is therefore required to truly establish its use in the high-field regime.

* Author to whom any correspondence should be addressed.



Original content from this work may be used under the terms of the Creative Commons Attribution 4.0 licence. Any further distribution of this work must maintain attribution to the author(s) and the title of the work, journal citation and DOI.

In this review, which is one of several on this broad subject [34–36], we discuss the key developments which have led to the success of the PCA. We begin in section 2 by discussing the basic concepts of PC emission in semiconductors, as well as considering THz-TDS. In section 3 we provide an up-to-date review of key active and substrate materials used for PC emission, subdivided by excitation wavelengths. In sections 4 and 5 we investigate the various electrode designs and innovations which have led to higher output powers and conversion efficiencies. In section 6 we discuss the excitations of PCA with amplified laser systems, which, when combined with more recent developments have led to significantly higher radiated electric fields. Finally, in section 7 we look to the future of PC technology.

2. Principles of photoconductive (PC) emission

The PCA is the most established and researched method of generating and detecting pulsed THz radiation [3, 37]. This is owing to its simplicity, ease of use, its reliability and relatively low cost. In its simplest form it uses readily accessible cleanroom materials, rudimental fabrication techniques and consists of a semiconducting material with two metallic contacts, separated by the PC gap (figure 1(a)). When the gap is illuminated by an ultrafast optical beam with photon energy typically greater than the bandgap of the semiconductor, free carriers are created resulting in an instantaneous drop in resistance of the device. THz emission relies on free carriers that are rapidly accelerated in opposite directions by a bias field applied between the electrical contacts. This effect is represented by the tilted bandstructure in figure 1(b). In many commonly used semiconductors, e.g. GaAs, the contribution from holes can be neglected as they have a significantly higher effective mass compared with electrons.

The transient current generated by the acceleration and subsequent recapture of the carriers radiates a quasi-single-cycle electromagnetic pulse at THz frequencies. An example of this is shown in figure 2(a), with the corresponding spectral components plotted in (b). The shape the THz waveform is dictated by the temporal evolution of the transient photocurrent within the material. The initial peak is a result of newly created photo-carriers being accelerated within the applied bias field. Its shape is therefore dependent on the length of the generating optical pulse, typically <100 fs for these purposes, the carrier mobility and saturation velocity of the material, as well as the screening of the bias field by the photocarriers. The amplitude of the second lobe is mainly driven by carrier recombination or capture by traps. The trailing oscillations shown in figure 2(a) are due to a low-pass filtering effect caused by a thick electro-optic (EO) crystal used in detection. As depicted in figure 1(a), the polarisation of the generated radiation is always parallel to the applied bias field. As the THz waveform, $E_{\mathrm{THz}}(t)$, is essentially the derivative of the generated photocurrent, $I_{\mathrm{pc}}(t)$, it can be expressed in the following terms [38]:

$$E_{\mathrm{THZ}}(t) = \frac{\mu_o \omega_o}{4\pi} \frac{\sin\theta}{r} \frac{\mathrm{d}}{\mathrm{d}t_{\mathrm{r}}} [I_{\mathrm{pc}}(t_{\mathrm{r}})]\,\theta \propto \frac{\mathrm{d}I_{\mathrm{pc}}(t)}{\mathrm{d}t} \qquad (1)$$

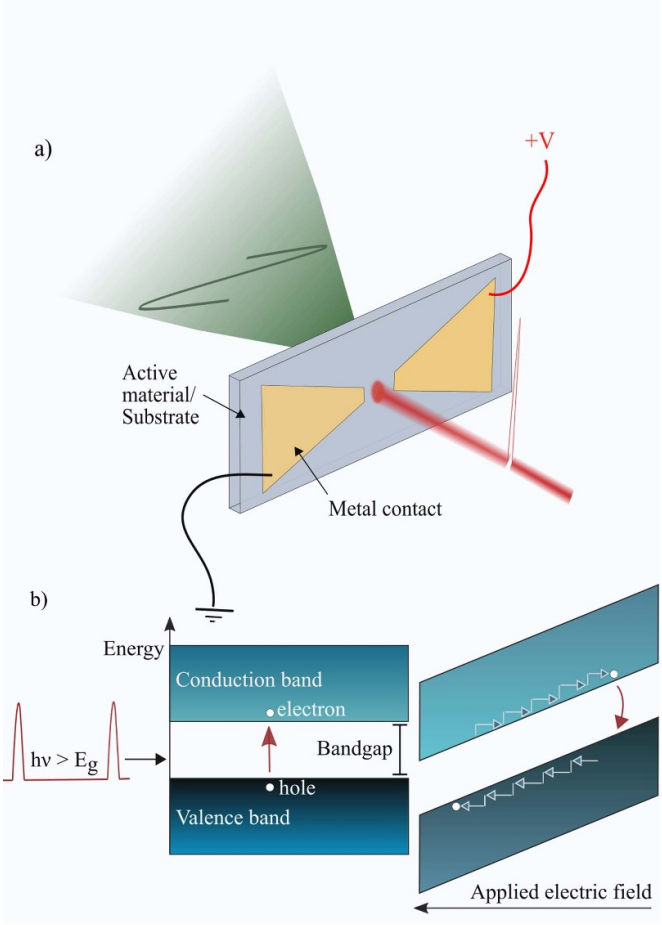


Figure 1. (a) A schematic of the THz generation process, the optical beam is shown in red, while the generated THz pulse is in green. (b) A simplified image of a semiconductor bandstructure, illuminated with an optical pulse and with electrical bias applied.

where μ_0 is the magnetic permeability of free space, ω_0 is the optical excitation spot size, and r and θ are the distance and angle (normal to the surface) from the device. This expression assumes a dipole approximately where the active region is significantly smaller than the emitter THz radiation wavelength. However, for larger devices of area A, such as those discussed in section 6, one could use equation (2) where z is the distance from the device and J_{s} represents the surface current density

$$E_{\mathrm{THZ}}(z,t) = -\frac{\mu_o A}{4\pi z} \frac{\mathrm{d}J_{\mathrm{s}}(t_{\mathrm{r}})}{\mathrm{d}t_{\mathrm{r}}}. \qquad (2)$$

The performance of an emitter, quantified through its THz output electric field or power, efficiency, bandwidth and signal-to-noise ratio (SNR), are all dependent on the material opto-electronic properties as well as the electrode geometry. Labels in figure 2 indicate how these values are extracted from the time-domain measurements. These properties include carrier mobility and lifetime, dark resistance, and breakdown voltage. Generally speaking, the radiated THz field is proportional to the generated photocurrent. However, the electrode geometry, contact design and substrate material all have a significant effect on the performance of the device. These, together with

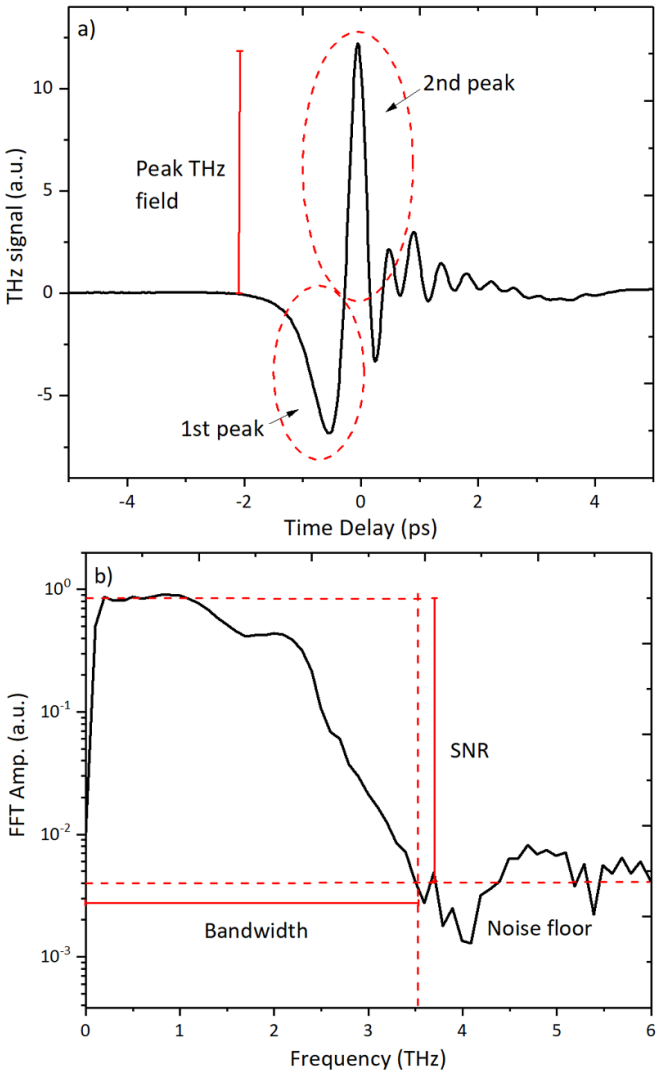


Figure 2. (a) THz pulse generated using a photoconductive emitter and electro-optically detected. (b) The FFT of the THz pulse. Both graphs highlight the generally accepted definition of quantities such as peak THz field, bandwidth and SNR. The SNR can also be extracted from the time-domain scans.

the various studied active materials, will be discussed in detail in sections 3 and 4.

2.1. Terahertz time-domain spectroscopy (THz-TDS)

THz TDS [4] is a widely utilized experimental technique employed for time- and phase-resolved detection and application of free-space THz radiation. The main function of the experimental setup is to study material properties such as complex refractive index and low energy interactions. THz-TDS (figure 3—main figure) has been a key technique to study and develop PC emitters over the past 30 years. In this technique, an ultrafast mode-locked laser delivers a beam that is split into a pump beam and a weak sampling beam. The pump is focused down to photoexcite the DC-biased PC emitter that generates a THz pulse. The pulse is collected, collimated and focused through a sample position using a pair of off-axis parabolic mirrors. A second set of mirrors is then used to focus the beam onto a detector. The weak sampling beam is directed through a delay stage to introduce a temporal delay relative to the THz pulse. The sampling beam is then focused down and spatially overlapped with the THz beam on the detector. When working with a high repetition rate oscillator laser, a PCA [39, 40] and EO-sampling [41] are the two most widely adopted methods for detection. Both sample the instantaneous electric field amplitude of the THz pulse with respect to the relative delay of the sampling pulse, allowing one to retrieve the THz pulse temporal waveform. For low-repetition rate amplified lasers, EO-sampling is widely used along with other methods of detection such as air-biased-coherent-detection which takes advantage of the high pulse energy [29]. Furthermore, for applications only requiring access to the THz intensity, it is possible to use a calibrated THz power-meter, a pyroelectric-detector or a helium-cool bolometer. We note here that the THz pulse can be collected from either side of the PCA after emission. In the case of transmission collection (figure 3—main figure), a Si hemispherical lens attached to the back of the device (non-illuminated side) can refract the forward propagating radiation allowing more to be collected from the first parabolic mirror. Reflection geometry (figure 3—inset), i.e. collecting the THz radiation from the same side of the device as photoexcited, is more commonly used in setups which require high bandwidths, as it avoids any dispersion or attenuation of the THz pulse propagating through the antenna substrate.

3. Materials for PC emission

The concept of THz generation through pulsed PC emission was first introduced and initially developed in the 1980s and 90s by Auston [42–44] and Grischkowsky [4, 37, 45]. Since then, a variety of different designs and materials have been investigated for this purpose. Throughout the literature, the terms ‘active material’ and ‘substrate’ are used interchangeably. In this article, unless a single-layer structure is discussed, we use the term substrate to refer to that underneath the active material, the active material being that which undergoes photoexcitation. A material well-suited for THz generation should have a high carrier mobility ensuring a high photocurrent [46], a low dark resistance to minimise current-induced heating, and a high breakdown voltage to allow high electrical field to be applied, increasing carrier velocity. Furthermore, a short carrier lifetime is desirable and results in a shorter current transient, producing a higher bandwidth THz pulse and protection against excess heating which can lead to early breakdown of the material. It is reported that too high a carrier mobility can also contribute to both heating and the early saturation of the PC properties [47, 48]. A compromise is therefore important and exact parameters can and should be tailored to the intended application. A summary of the advantages and disadvantages of the key materials discussed in this section is given in table 1.

3.1. 800 nm pumped materials

3.1.1. Semi-insulating (SI) GaAs. Several of the early studies on PC emission were conducted using various forms of

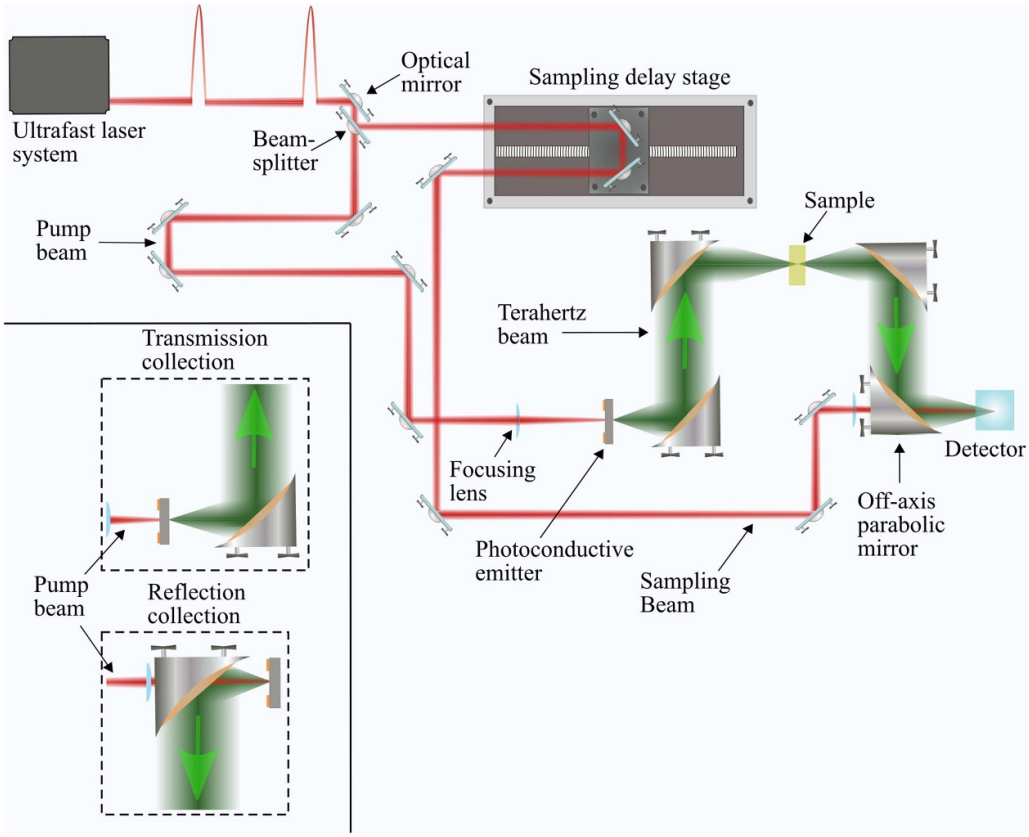


Figure 3. Terahertz time-domain spectroscopy setup displaying a transmission collection geometry. The red beam represents the ultrafast laser pulses, while the green beam represents the THz radiation, with arrows indicating the direction of travel. Inset in the bottom left-hand corner illustrates two separate THz collection techniques, transmission and reflection collection geometries.

silicon-on-sapphire (SOS) including doped with Ar^+ [44, 68], undoped [37] and radiation-damaged [69, 70]. However, it became clear that gallium arsenide (GaAs) possesses superior characteristics for PC emission with a faster response time owing to its higher mobility [71]. Furthermore, with a direct bandgap of 1.42 eV at room temperature [72], it can be effectively photoexcited at 800 nm, making it compatible with titanium (Ti)-doped sapphire laser technology. SI-GaAs [73–76] is typically grown using liquid encapsulated Czochralski method at 450 °C–600 °C [49, 77], a high temperature that ensures a single crystal growth. This results in a reliable, reproducible, and commercialised growth procedure, which has led to SI-GaAs becoming the most widely utilized and researched materials for PC emission. It typically has a carrier mobility of between 4200 and 6000 $cm^2\ Vs^{-1}$ [49, 78] and trapping time of greater than 100 ps [79, 80].

3.1.2. Low-temperature (LT)-grown GaAs. LT-grown-GaAs [71, 81–85] has also proved very successful for PC emission. In 1988, it was discovered by Smith *et al* [81] that by reducing the growth temperature to between 200 °C and 300 °C and growing in an arsenic rich environment, the resultant crystalline material retains a carrier lifetime two-orders-of-magnitude shorter than that of SI-GaAs [50]. It also exhibits a higher resistivity and breakdown field when annealed at higher temperatures [1, 51]. While LT molecular beam epitaxy (MBE) growth of materials is difficult owing to unreliable temperature monitoring below 400 °C, the highly desirable attributes of LT-GaAs are a direct result of excess As precipitants, which develop when the material is annealed from point defects, such as As antisites, As interstitials, and Ga vacancies formed in growth [83].

Early publications using LT-GaAs demonstrated the improved performance it can offer over SI-GaAs and SOS [71, 82, 86]. A direct comparison of LT-GaAs and SI-GaAs was conducted by Tani *et al* [1]. When exciting each device with 80 fs wide pulses at a frequency of 780 nm, they demonstrated that the SI-GaAs device outputted significantly more power than that of the LT-GaAs when biased below 30 V, attributed to the high mobility carriers in SI-GaAs. However, for higher biases the dark current in the SI-GaAs drastically increases, resulting in an avalanche effect and the breakdown of the material at 100–140 $kV\ cm^{-1}$ across a 5 μm wide gap. In comparison, the equivalent LT-GaAs device broke down at 200 $kV\ cm^{-1}$. The distinction in photocurrent between the two materials is highlighted in figure 4. These results were confirmed by Stone *et al* [87] who suggested that while the thermal runaway of a device is dependent on optical power and active area, it is significantly higher for LT-GaAs-based-devices, owing to the reduced carrier mobility (120–200 $cm^2\ Vs^{-1}$ [84]) resulting in lower photocurrent and reduced ohmic heating [88].

Table 1. Summary of the main materials tested for the PC emission at various wavelengths.

Material	Optimum excitation wavelength (nm)	Advantages	Disadvantages	Key attributes
SI-GaAs	800	Commercially available, reproducible wafer performance. High carrier mobility.	Early optical saturation, relatively low resistivity and breakdown bias.	Carrier mobility of 6000 cm^2 Vs^{-1} [49]. Breakdown at 140 kV cm^{-1} (5 μm gap) [1].
LT-GaAs	800	High breakdown/saturation relative to SI-GaAs.	Difficult to grow, optimise and reproduce.	100 fs carrier lifetime [50], breakdown field as high as 340 kV cm^{-1} [51].
Light and heavy ion implanted GaAs (As^+/O^+/H^+/C^+)	800	Good control and reproducibility. Higher saturation threshold relative to SI-GaAs [52].	Requires expense equipment for ion implantation.	300 fs carrier lifetime (As^+) [53]. Breakdown of 14 kV cm^{-1} (O^+) and 12.5 kV cm^{-1} (As^+).
GaBiAs	1030	Already being used in commercially available PCAs.	Requires low-temperature MBE growth before 400 °C.	Conversion efficiency of 5×10^{-4} [54].
InAs QD:GaAs	1100–1300	Can sustain high optical density (450 μJ cm^{-2} [55]) and exhibits a superlinear response as a function of pump intensity.	Requires QD optimisation and an optical parametric oscillator/amplifier to pump resonantly.	Exhibits a reduction in lifetime with increased pump power [56].
Au doped Ge	1100–1550	Capability of gapless bandwidths exceeding 70 THz owing to the lack of LO modes in the THz region.	Not fully researched, longer lifetimes >300 ps.	High bandwidths (70 THz) and peak field of 0.8 kV cm^{-1} [57].
Fe doped InGaAs	1550	High resistivity [58]. Can be grown by CVD [59].	Relatively low mobility owing to increased scattering [59].	High resistivity 10^7 Ω cm [60].
Rh doped InGaAs	1550	Capable of very high output powers and conversion efficiencies. High mobility carrier [61].	Requires further investigation into the incorporation of Rh in the MBE growth process.	High output powers and conversion efficiencies of 637 μW and 3.4% [61].
InGaAs/InAlAs heterostructures	1550	Potential for high conversion efficiency and output power. Very short carrier lifetimes.	Complex material growth, requires further research.	64 μW output power and 2×10^{-3} conversion efficiency [62]. Carrier lifetimes of 113 fs [63].
ErAs/InGaAs heterostructures	1550	ErAs nanoparticles have high stability, very short carrier lifetimes [64].	Complex material growth, requires further research.	200 fs carrier lifetime and high mobilities of 1800 cm^2 Vs^{-1} [65].
ErAs QD:GaAs	1550	High conversion efficiency and output power.	Requires optimisation as it is a new material.	High output powers of 117 μW and conversion efficiency of 0.2% [66]. Breakdown at 100 kV cm^{-1} [67].

There have been many publications helping to explain the emission characteristics and carrier dynamics of LT-GaAs [72, 83–85, 89–94]. An early study into the material characteristics by Gupta *et al* [84] demonstrated an increase in carrier lifetime as a function of growth temperature. This trapping time was later proven, via transmission electron microscopy (TEM) and pump-probe spectroscopy, to be proportional to the average distance between the As precipitants [85]. More details on the role of As precipitants in carrier trapping were provided by Lochtefeld *et al* [83] who revealed that the mechanisms for recombination differ greatly before and after annealing. Prior to annealing, the full carrier recombination is a two-step process, with the initial carrier trapping and eventual electron–hole recombination occurring on the order of 100 fs and 1 ns respectively. After annealing, the As precipitates dominate the process with full recovery occurring on the order of 1–20 ps, depending on the initial excess As incorporated in growth.

In 2014 Moon *et al* [95] used this knowledge to explain how growth and anneal temperatures effect the performance of the PCA. Two LT-GaAs wafers grown at 200 °C and 230 °C were both subjected to annealing from 500 °C to 620 °C before being used to fabricate PC emitters with dipole antennas. They establish that for the wafer prepared at the highest growth and anneal temperatures, the excess As is completely depleted post

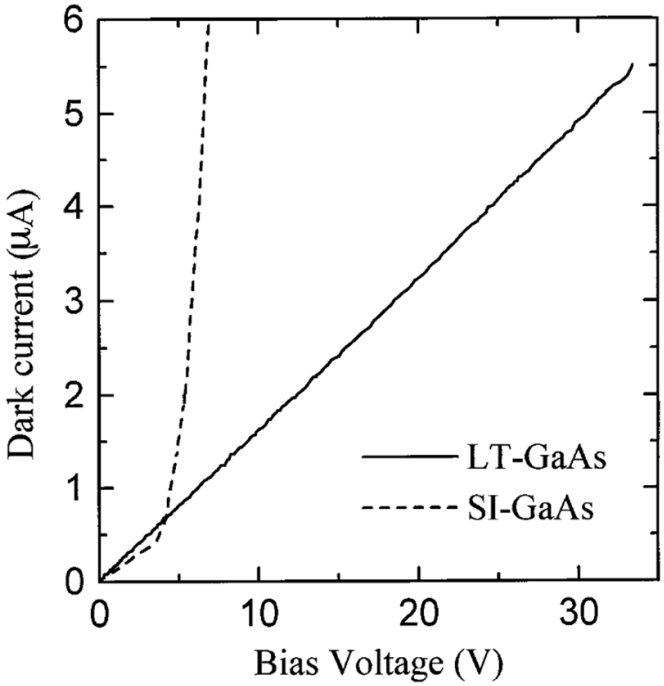


Figure 4. *I–V* curves measured for 5 μm gaps of LT-GaAs and SI-GaAs. Reprinted with permission from [1]. © The Optical Society.

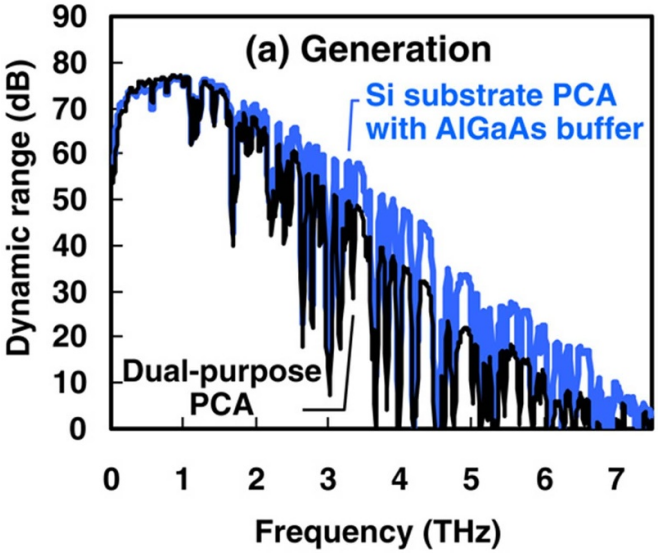


Figure 5. THz spectra generated from Si substrate PCA with AlGaAs buffer layer (blue line) and dual-purpose PCA (black line). The detector used was a dual-purpose PCA. Reproduced from [46]. © IOP Publishing Ltd. All rights reserved.

anneal. The increase in anneal temperature has two significant effects; firstly it increases the size of the precipitants clusters, also seen in by Harmon *et al* [85]. Secondly, it decreases As antisite density, suppressing the carrier hopping and increasing the resistance of the material. The devices are tested for both PC emission and detector in a TDS system. While an optimum anneal temperature of 580 °C is determined for detection, this temperature seemed to have very little effect on the emission characteristics of the device. They declare that the optimum anneal temperature for an LT-GaAs wafer is heavily dependent on its initial As density, which is determined by its growth conditions. However, to ensure a high dynamic range for PC emission, Kamo *et al* [46] determined a lifetime of 10–20 ps to be optimal. In this study that corresponds to a growth and anneal temperature of 300 °C and 600 °C respectively.

3.1.3. LT-GaAs on insulating substrates. For many of the studies discussed above LT-GaAs was grown using MBE, either directly onto an SI-GaAs wafer or with a thin epitaxial layer of AlAs or AlGaAs between active material and substrate. Unfortunately, as SI-GaAs possesses carriers with a significantly higher mobility and longer lifetime, as well as characteristic lower breakdown field, this has a detrimental effect on the device as it makes it susceptible to being overbiased. To avoid this, an advantage can be gained by replacing the SI-GaAs substrate with a THz transparent insulating material. However, due to mismatches in the lattice constant resulting in lattice dislocations in the LT-GaAs, growing directly onto these substrates is very challenging. This was first attempted in 2004 by Ma *et al* [96] who grow a LT-GaAs film at 250 °C directly onto a Si wafer using MBE. When tested in an TDS system, the device showed a very similar response to that of LT-GaAs grown on SI-GaAs, which suggests that any dislocations in the LT-GaAs do not limit the emission properties of the device. In 2014, Kamo *et al* [46] successfully grew LT-GaAs onto a high-resistivity Si wafer with the addition of a 200 nm thick heteroepitaxial AlGaAs layer. This allows them to avoid dislocations in the LT-GaAs, while the larger bandgap of 2 eV helped to electrical isolate the active material and substrate. When tested in emission against LT-GaAs-on-SI-GaAs, this unique material combination resulted in substantially better performance at frequencies above 2 THz, owing to higher transmittance of THz radiation through the Si substrate. The full spectral response from the two devices is shown in figure 5.

An alternative approach, coined by Yablonovitch *et al* [97], is to chemically etch the thin epitaxial layer. It can then undergo epitaxial liftoff (ELO) from its growth substrate and van der Waals forces can be used to bond the LT-GaAs film, typically 0.5–3 μm thick, to a new host substrate. This technique has been shown to work with various materials including Si [98], glass [99, 100], sapphire [99–101], quartz [102], $LiNbO_3$, InP, and diamond [103]. In the early works of Heiliger *et al* [99, 100], 0.5 μm thick LT-GaAs films were transferred onto both sapphire and glass substrates. Metal dipole antennas were fabricated on top of the LT-GaAs and the devices were tested in both a free-space (sapphire) and 'on-chip' (glass) geometry [104, 105]. The sapphire-mounted device showed a five-fold-increase in peak output signal over the equivalent SOS device.

Further work by Awad *et al* [101] and later by Rios *et al* [98, 106] both revealed how this bonding technique can be used to construct PCA array features. In the latter of these, 2 μm thick LT-GaAs is removed from its SI-GaAs growth substrate and bonded with SiO_2-on-Si [106]. This was used to form a coplanar patch PCA array with a grid of 20 μm

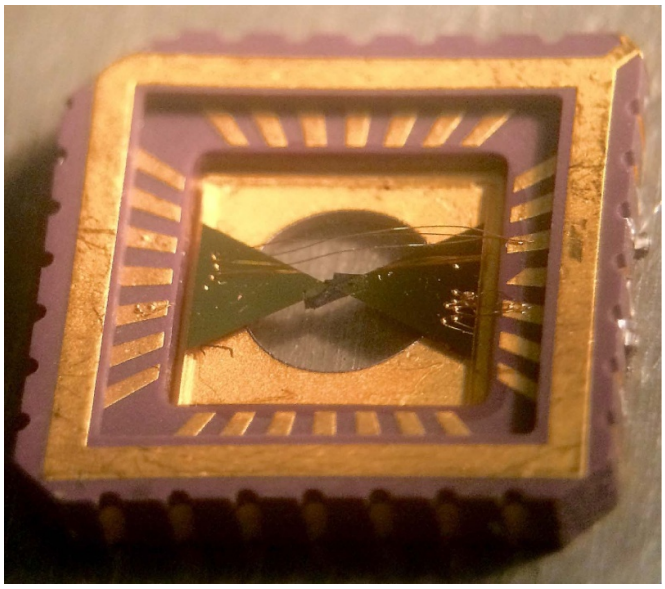


Figure 6. Microscope image of a PC emitter fabricated using LT-GaAs-on-quartz.

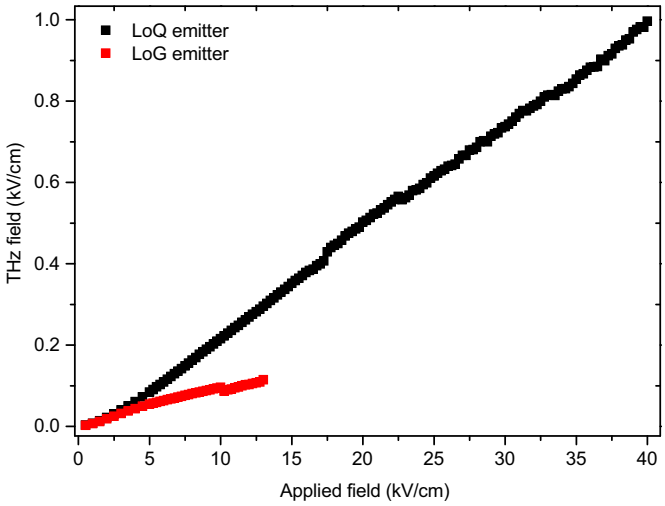


Figure 7. Comparison of THz output field as a function of applied bias for LT-GaAs-on-quartz (LoQ) (black) and LT-GaAs-on-SI-GaAs (LoG) (red). Reprinted with permission from [102]. © The Optical Society. CC BY 4.0.

wide bowtie devices. Lastly in 2016, Bacon *et al* [102] used the ELO technique to construct a LT-GaAs bowtie structure on various thicknesses of *z*-cut quartz substrate. A microscope image of this device is shown in figure 6. In comparison with the THz emission characteristics of the 'as-grown structure', LT-GaAs/AlGaAs/SI-GaAs, this unique device was able to sustain significantly higher bias fields owing to the removal of the SI-GaAs substrate. It was shown that excess heating, caused by photoexcited carriers in the optically sensitive SI-GaAs substrate, resulted in the early saturation and breakdown of the device [51, 107]. Replacing the 500 μm thick SI-GaAs with a 2 mm thick quartz substrate, resulted in three-orders-of-magnitude greater dark resistance and an eight-fold increase in output field as a function of bias (figure 7), when tested in a TDS setup with reflective-collection geometry.

3.1.4. Ion implanted GaAs. An alternative method to decrease the carrier lifetime of GaAs and to improve its emission characteristics is through ion implantation [108, 109]. This process involves bombarding the material with a known flux of high-energy ions. After its initial demonstration by Johnson *et al* [108] in 1989, proving that implanting H^+ ions into GaAs could reduce its carrier lifetime to sub-picosecond, this led to multiple groups replicating the characteristics of LT-GaAs through As^+ ion implantation [110, 111]. This technique provides precise control over the ion dosage making it more reproducible than LT growth. The first full characterisation of a PCA fabricated on GaAs:As^+ was reported in 2003 by Liu *et al* [53]. In this work a SI-GaAs substrate was bombarded with arsenic ions at doses of 10^{16} ions cm^{-2}, prior to a dipole antenna being fabricated on top. After annealing, this material not only retained a carrier lifetime of 0.3 ps, it possessed a five-fold increase in resistivity compared with unprocessed SI-GaAs, owing to the formation of arsenic precipitates. As illustrated in figure 8, the shorter carrier lifetime in GaAs:As^+ results in a shift in the peak of the FFT spectrum to higher frequencies. This contributes to a larger second peak in the temporal waveform (a). The GaAs:As^+ device also shows a higher breakdown field and later saturation as a function optical power, compared with SI-GaAs. This material therefore revealed similar behaviour to that of LT-GaAs owing to the low carrier mobility of GaAs:As^+ (150 cm^2 Vs^{-1}), as this is inversely proportional to saturation fluence [47, 112].

Since then it has been demonstrated that the use of multi-energy-implanted As^+ ions provide a shorter THz pulse and a higher bandwidth response, relative to single-energy ions [113]. Furthermore, the implantation dose has a significant effect on the spectral peak of the PC response, with a rise in As^+ ion density from 10^{13} to 10^{16} cm^{-3} resulting in a shift from 1.4 to–2.2 THz [114]. This is attributed to shorter trapping times and higher vacancy concentrations with increased ion density.

In 2005 Salem *et al* [52, 115, 116] began experimenting with the GaAs implanted with various other ions including H^+, O^+ and N^+. In [52], their THz generation properties are compared with both GaAs:As^+ and unprocessed GaAs antennas, all of which were tested with a 120 μm wide antenna slot design. They showed that all devices, with the exception of GaAs:N^+, saturated at a higher optical fluence than non-processed GaAs emitter. A further study on THz emission from GaAs:N^+ conducted by Winnerl *et al* [117] revealed that the radiated THz signal was inversely proportional to the doping concentration. This is attributed to reduced mobility and carrier lifetime at higher doping levels.

Lastly, in 2014 Singh *et al* [48] irradiated GaAs with carbon, as using a light ion such as H^+ with a low dose can result in high THz emission [52]. C^+ ions were implanted with doses ranging from 10^{12} to 10^{15} cm^{-2}. It is shown in figure 9 that the irradiated sample with a dose of 10^{14} cm^{-2} can sustain an impressive seven-fold increase in bias field, compared with the non-irradiated GaAs wafer. This is owing

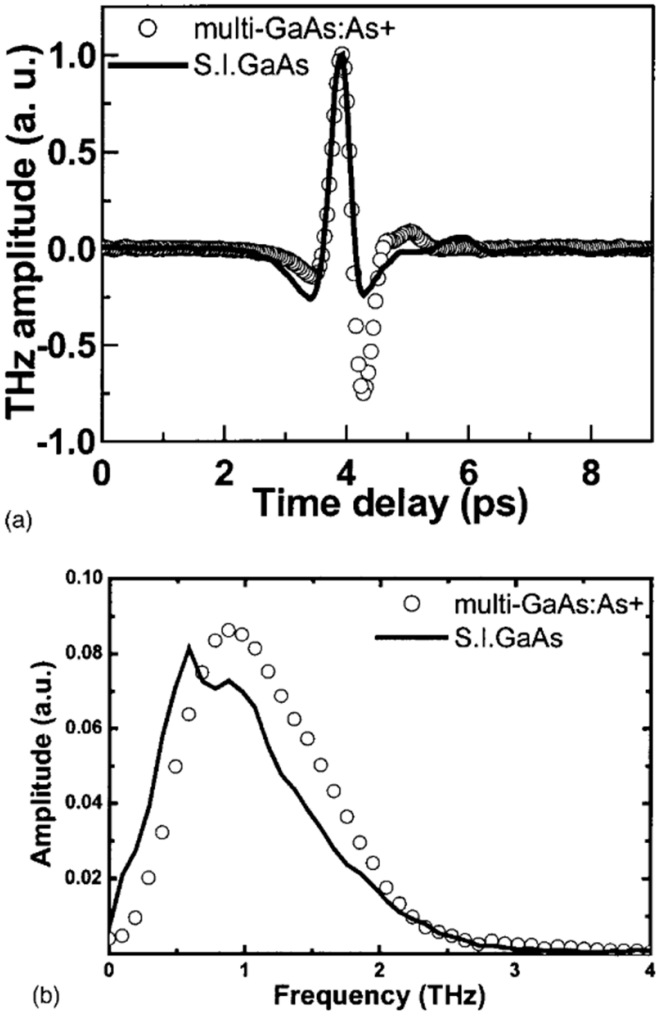


Figure 8. THz radiation pulses from small gap (5 μm order) photoconductive antenna fabricated on multi-implant GaAs:As$^+$ solid curve and SI GaAs (dashed curve). (b) Fourier-transformed amplitude spectrum of (a). Reproduced from [53], with the permission of AIP Publishing (DOI: 10.1063/1.1541105).

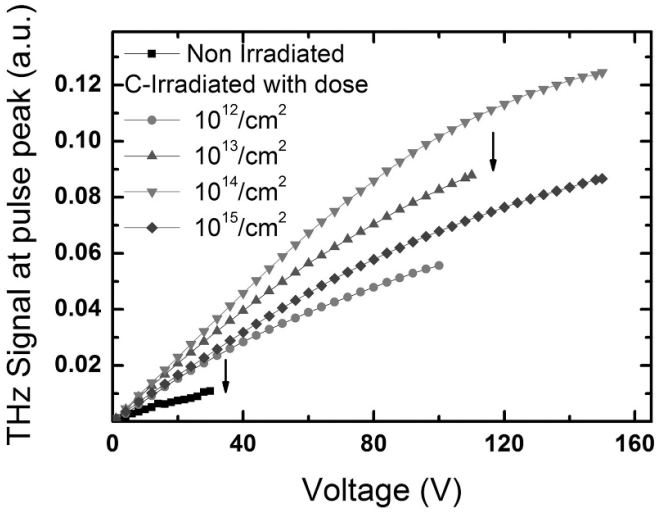


Figure 9. Variation of emitted THz pulse amplitude with applied bias from non-irradiated and carbon-irradiated SI-GaAs sources. The breakdown voltage for non-irradiated sample is the lowest 30 V and for the higher dose is more than 150 V (arrows). Reproduced from [48], with the permission of AIP Publishing (DOI: 10.1063/1.4864623).

to the sub-picosecond trapping times and diminished heating effects, resulting from two-orders-of-magnitude reduction in dark current. Due to the implantation of the C^+ ions in the GaAs, the device was able to emit approximately 100 times the output power. This article, combined with the previously published body of work, provide exciting evidence of the advantages of ion implantation in GaAs. However, for more information please read [118], a review of ion-implantation for THz applications.

3.2. 1030 nm pumped materials

While much of the research into PCA has been focused on pumping at 800 nm, there has been a rise in the number of studies using excitation at longer wavelengths. This is partly owing to the development of Yb-doped fibre technology [119], resulting in compact short-pulse mode-locked lasers operating with an emission wavelength centred at 1030 nm. This typically has significantly higher electrical-to-optical conversion efficiency, compared with Ti:sapphire technology [120]. While untreated GaAs has too large a bandgap to be effectively photoexcited at this wavelength, other materials proposed include GaBiAs [54, 121–123], LT-grown InGaAs [124, 125], various InGaAs-based heterostructures [126, 127] and GaInAsBi [128]. However, InGaAs has proven undesirable at this wavelength owing to its low bandgap energy of 0.55 eV at 300 K [129]. This has been shown to increase carrier lifetime as hot electrons are photoexcited directly into energy states significantly higher than the conductive band edge [126]. However, GaBiAs has been established as an effective and commercially viable material at this wavelength for several key reasons. Firstly, the material bandgap is a function of the bismuth concentration [121], meaning that it can be engineered for a desired excitation energy. Secondly, much like LT-GaAs, its growth conditions can be optimised for short carrier trapping times, with LT growth providing lifetimes as short as 1 ps [122, 123]. This material has demonstrated optical-to-THz conversion efficiencies exceeding 10^{-4} and emission bandwidth greater than 3 THz [54].

3.3. 1100–1300 nm pumped materials

Until recently there has been little interest in photoexciting in this wavelength range. Unlike at other wavelengths, where the use and development of a PC material is driven by laser technology, here the discovery of PC emission from materials such as GaAs incorporating InAs quantum dots (QDs) has prompted a shift in excitation to longer wavelengths [55, 56, 130–133]. The reason for this is to enable resonant excitation within the InAs QD structures. A schematic of this type of device is shown in figure 10(a), while a TEM image of an individual QD is shown in (b). The incorporation of 1–2 nm thick InAs QDs layers into bulk GaAs has been shown as an effective

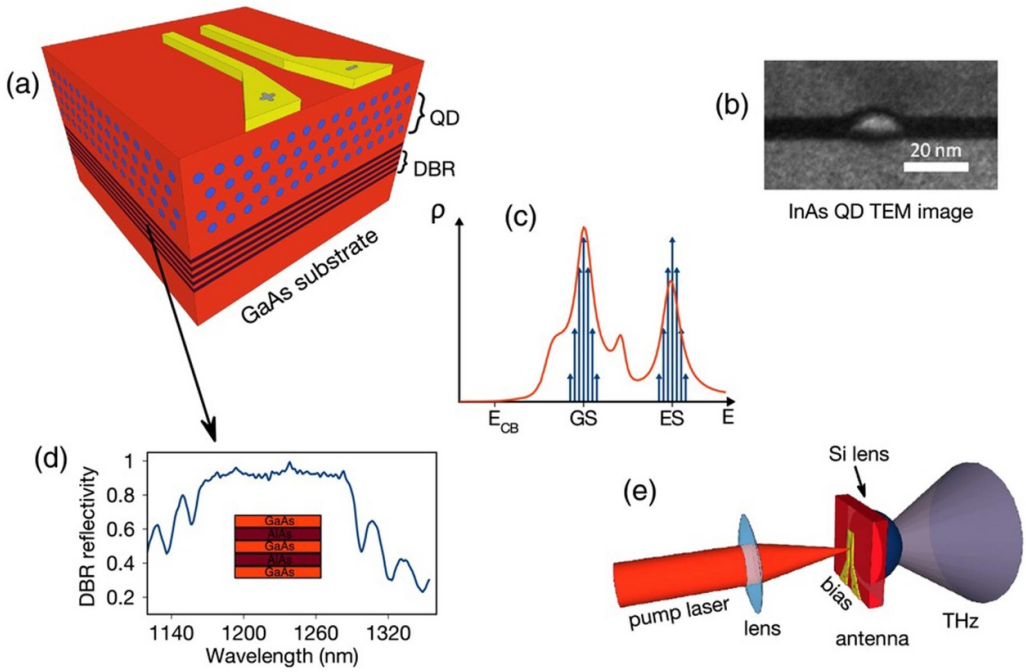


Figure 10. (a) Structure of quantum dot photoconductive antenna, QD—active region with several layers of InAs quantum dots implanted into GaAs matrix, DBR—distributed Bragg reflector; (b) cross-section TEM measurement of an InAs QD; (c) quantum dot material density of states, ECB—bottom of the conduction band, GS and ES—ground and excited states energies correspondingly, red line shows material photoluminescence spectrum; (d) reflectivity and schematics of AlAs/GaAs distributed Bragg reflector used in the antenna; (e) schematic of THz generation in the PCA. This image is recreated from figure 1 [55], under the following licence (https://creativecommons.org/licenses/by/4.0/legalcode). Reproduced from [55]. CC BY 4.0.

means of reducing carrier lifetime, while maintaining a high mobility [55, 132]. This is due to the immediate capture of photoexcited carriers within the excited states of QD (ES in figure 10(c)). As a consequence, a rise in optical pump power results in a reduction in carrier lifetime due to the onset of stimulated transitions [132].

This unique attribute has several interesting effects. Firstly, an increase in optical pump power results in a rise in saturation bias field, this is typically not observed in bulk devices [134]. Secondly, the shorter carrier lifetime results in both increased signal at higher frequencies and the ability to sustain greater optical intensities prior to breakdown, compared with LT-GaAs devices [133]. The optical-to-THz conversion efficiency of the material can be improved by optimising the uniformity of QD sizes and the inter-QD spacing.

3.4. 1550 nm (telecommunication-wavelength) pumped materials

Another avenue of interest for PC emission is the use of optical telecommunication wavelengths for photoexcitation, allowing for future integration of THz devices and taking advantage of the stable and low-cost fibre-based technologies. Due to low-pulse dispersion, limited attenuation and a set gain spectrum when pumped at 980 nm, Er-doped fibre-optic oscillators and amplifiers generate a wavelength at approximately 1.55 μm [135]. Many materials such as InAs [136], InSb [137, 138], GaSb [139], InGaAsP [140], GaInAsBi [141] and doped InGaAs [58, 142, 143] have all been investigated for this purpose. A recent addition to this list is Ge:Au which has demonstrated impressive gapless bandwidths of up to 70 THz. This result is due to the fast acceleration of high mobility carriers (3900 $cm^2\ Vs^{-1}$) excited with an 11 fs long optical pulse, as well as weak absorption from transverse optical phonon modes from the crystal lattice [57, 144].

3.4.1. Doped InGaAs. Doping is considered relatively important in InGaAs as it typically has a low dark resistance, owing to its small bandgap compared with GaAs, and a relatively long lifetime [145]. In one of the earliest studies, Suzuki *et al* [146] compared PCAs fabricated on $In_{0.53}Ga_{0.47}As$:Fe in its doped and undoped form, both grown using chemical vapour deposition. The doped layers were implanted with Fe ions at the dose of $1 \times 10^{15}\ cm^{-2}$, producing an amorphous layer at the surface of the sample. It was found that the doped sample had a faster response time than its undoped counterpart, which was explained by a carrier gradient forcing electrons into the amorphous area where they undergo ultrafast relaxation due to Fe ions acting as deep accepter states in the material bandgap [147]. This is indicated by both the reduced temporal width and the small negative peak in the Fe-implanted time-domain trace plotted in figure 11. The doped sample also experiences an increase in resistivity and reduction in carrier mobility of greater than six times, down from 9900 to 1500 $cm^2\ Vs^{-1}$, resulting in a higher saturation fluence.

Since then various publications have studied Fe-doped InGaAs as a PC material [59, 60, 143, 148]. For instance,

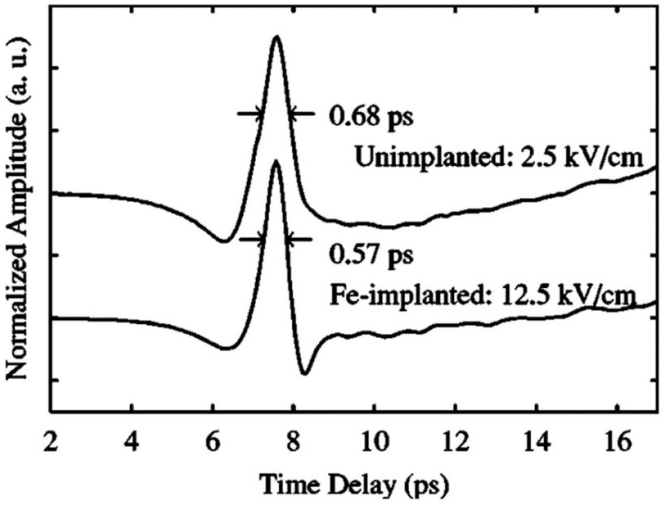


Figure 11. Normalized waveforms of terahertz radiation from implanted and unimplanted InGaAs emitters. Excitation powers of implanted and unimplanted emitters is 5 mW. Reproduced from [146], with the permission of AIP Publishing (DOI: 10.1063/1.1861495).

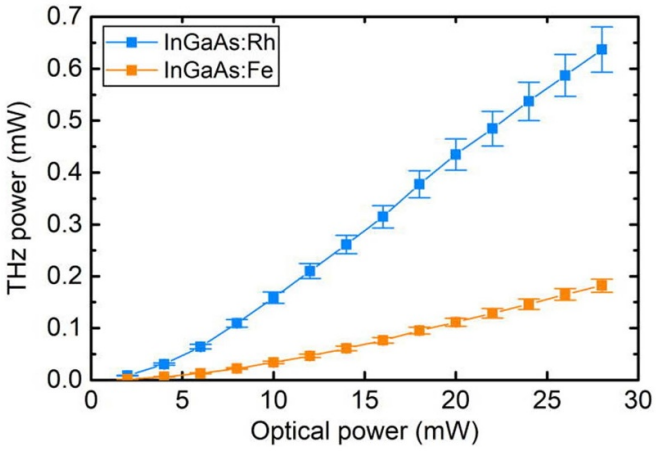


Figure 12. Absolute emitted THz power as a function of optical power for Rh and Fe doped InGaAs for a constant 60 kV cm^{-1} bias. A pyroelectric thin-film detector calibrated by the German Metrology Institute PTB was used for the measurements. Reproduced from [61], with the permission of AIP Publishing (DOI: 10.1063/5.0020766).

Wood *et al* [149] showed that precise control of the Fe-doping can be achieved if added during the epitaxial growth process. A comparison of multiple InGaAs:Fe wafers, doped with concentrations between 2×10^{16} and 5×10^{18} cm^{-3}, revealed that the THz output power is inversely proportional to the doping level. This is attributed to reduced scattering, increasing both carrier mobility and photocurrent. A recent study of InGaAs:Fe conducted by Globisch *et al* in 2017 [143], found that through optimisation of growth and anneal temperature (400 °C and 600 °C respectively), a carrier lifetime and mobility of 300 fs and 900 cm^2 Vs^{-1} were realised, resulting in a peak output power of 75 μW.

As well as iron, InGaAs has also been doped with heavier ions such as As$^+$ [150] and Br$^+$ [151, 152], the latter of which revealed a very short carrier lifetime of less than 200 fs and a reduced carrier mobility of 490 cm^2 Vs^{-1}, owing to increased scattering with doping dose of 1×10^{12} cm^{-2}. The performance also depends heavily on the materials In/Ga ratio [153], but has proved comparable to that of LT-GaAs when excited at a wavelength of 800 nm [148]. Kohlhaas *et al* [61] recently demonstrated a significant step forward by showing that MBE-grown Rhodium doped InGaAs can be used to generate an impressive 637 μW of THz power, over a bandwidth of 6.5 THz. A combination of high mobility (>3000 cm^2 Vs^{-1}), high resistivity and sub-picosecond lifetimes resulted in an optical-to-THz conversion efficiency of 3.4%. Furthermore, the Rh doped material was shown to have an output power 3.5 times that of the same device fabricated on InGaAs:Fe. This comparison is displayed in figure 12 as a function of optical excitation power. InGaAs has also been compared directly with other semiconductors such as InSb and InAs, for a range of excitation wavelengths from 780 to 1650 nm [154]. This study reveals that for all materials the amplitude of the THz output field is dependent on the excitation wavelength, with InSb performing best at 1650 nm. However, increasing photon energy sees a significant rise in output power from the InGaAs emitter and a substantial drop in that of InSb due to exciting electrons into high-energy low mobility valleys.

3.4.2. InGaAs/InAlAs heterostructures. Heterostructure devices comprised of InGaAs/InAlAs multilayer stacks have been proposed by several groups [62, 155–158]. In this structure 8–10 nm thick optically transparent (at 1550 nm) InAlAs layers act to increase the overall dark resistivity of the InGaAs, as they possess a high concentration of deep electron traps and have a wider bandgap [157]. Sartorius *et al* [155] demonstrated an increase in resistivity of four-orders-of-magnitude over bulk InGaAs by growing the structure at low temperature (<200 °C) to decrease recombination times through incorporation of excess As_{Ga} trapping sites. Furthermore, this technique of physically separating the active and trapping material has proven to yield comparable results in THz bandwidth to that of LT-GaAs excited at 800 nm, suggesting that they provide similar trapping times [157]. It was demonstrated that this structure can yield impressive THz fields as high as 2.5 kV cm^{-1} [158] and a peak output power and efficiency of 64 μW and 2×10^{-3} [62] respectively. This was achieved by optimising the growth temperature and domain thickness of the heterostructure, such that InGaAs has a high mobility while InAlAs has a high defect density. For a full review article on optical excitation at longer wavelength please read [159].

3.4.3. ErAs materials. ErAs is another well-researched dopant used in both GaAs [66, 160–162] and InGaAs [65, 67, 145, 163–165], as it is known to work effectively as an ultrafast trapping site [163]. Early publications with ErAs discuss the creation of self-assembled metal nanoparticles or 'nanoislands' [160]. These can be incorporated into InGaAs-based superlattice heterostructures to promote subpicosecond lifetimes [65, 163]. An example of this type of device was

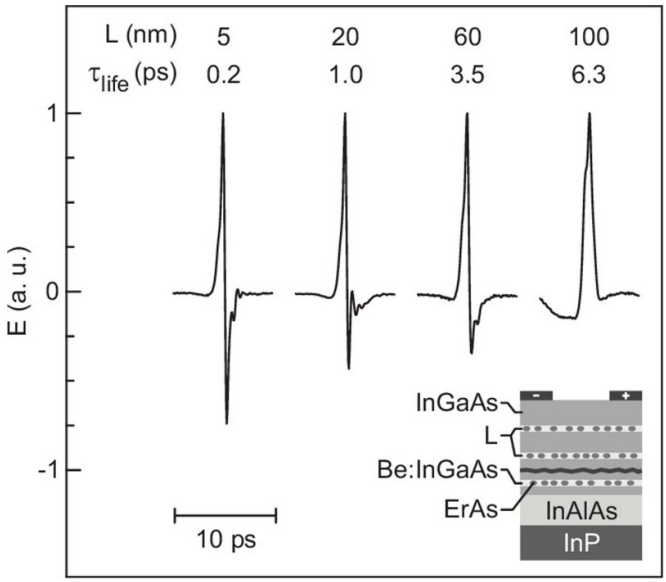


Figure 13. Normalized pulse forms emitted by photoconductive antennas based on ErAs:$In_{0.53}Ga_{0.47}As$ superlattices with different superlattice periods L and electron lifetimes τ_{life}. The inset shows a vertical cross-section of an ErAs:$In_{0.53}Ga_{0.47}As$ superlattice. Reproduced from [145], with the permission of AIP Publishing (DOI: 10.1063/1.3374401).

published in 2010 by Schwagmann *et al* [145], who grew a superlattice structure (shown in figure 13) formed from alternating layers of self-assembled ErAs islands within bulk InGaAs:Be, and undoped 'spacer' InGaAs. The P-doped layers act as both trapping sites and increase overall resistivity of the structure. Figure 13 also displays four separate THz pulses generated by optically exciting this structure at 1550 nm. It is clearly shown that by increasing the InGaAs domain length (L) within the structure, the excited electrons are required to travel further before recombining in the ErAs trapping layers. This increases the carrier lifetime and reduces the magnitude of the second peak of the THz waveform. A similar structure allowed them to demonstrate the dependence of device resistivity on domain length [65].

Recently this focus has shifted with the study of ErAs QD's in both GaAs [66, 161, 166] and InGaAs [67, 165]. It has long been established that doping GaAs above the solubility limit of 7×10^{17} cm^{-3} at a growth temperature of 580 °C results in the creation of near-spherical QD structures [162]. These artefacts bring about an extrinsic photoconductivity within the material, as electrons are photoexcited directly out of mid-bandgap QD states into the conduction band before undergoing ultrafast relaxation. This mechanism occurs resonantly at 1550 nm and has resulted in optical-to-THz conversion efficiencies as high as 0.18% [161]. Furthermore, a recent study by Zhang *et al* [66] has demonstrated the use of 'superradiance', an effect where the PC properties of a material are enhanced by cooperative spontaneous emission brought about a strong population inversion within the QDs [167]. This contributed to record output powers of 117 μW for this material but a similar conversion efficiency as previous studies [161].

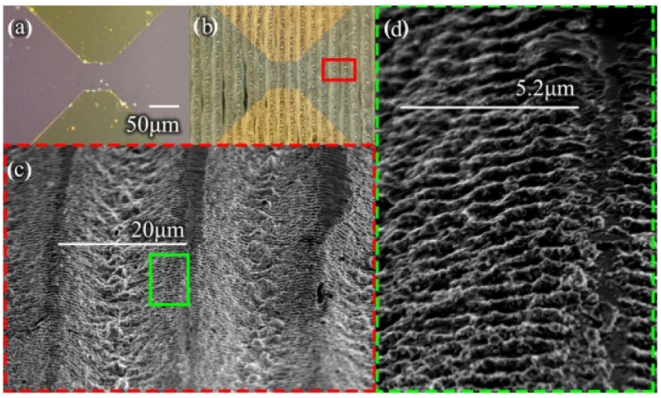


Figure 14. Optical microscope images of (a) nonablated GaAs and (b) femtosecond-laser-ablated photoconductive antennas. (c) SEM picture of the area within the red rectangle of (b) showing 20 μm wide grooves. (d) Zoom within the green rectangle of (c) showing the formation of ripples. Reprinted with permission from [169]. © The Optical Society.

A full comparison of ErAs:GaAs and InGaAs for 1550 nm excitation can be found in [168].

3.5. Comparison of the reviewed materials

The key materials discussed within this section are summarised in table 1 below.

3.6. Surface texture

There have been several studies investigating the effect of varying the surface texture of the active material on the characteristics of the THz emitter [169, 170]. Madéo *et al* [169] showed that systematically ablating of SI-GaAs, using high intensity optical excitation, enhances the photo-absorption of the material. Optical and SEM images of the modified material are presented in figures 14(b) and (c) respectively. When compared with the non-ablated material for PC emission, the ablated GaAs demonstrates a lower photocurrent and mobility owing to the shortened carrier lifetime (figure 15(c)). However, as can be seen from the THz time-domain traces plotted in figure 15(a), when excited at high optical intensities of 10 mJ cm^{-2}, the increase in absorption results in a 65% rise in conversion efficiency. This is not the case for lower optical intensities owing to the effects of free carrier absorption arising from the ablation process. A related study was also conducted by Collier *et al* using InP as the active material [170]. In this instance, the material was mechanically polished with different grit-size to achieve different textured surfaces with fine and course roughness. Similar to the findings in [169], texturizing the surface of the material increases the optically excited surface area, while decreasing the carrier lifetime an order-of-magnitude due to contributions from surface recombination. This results in a similar reduction in photocurrent in the textured samples, as well as rise in resistance and breakdown voltage.

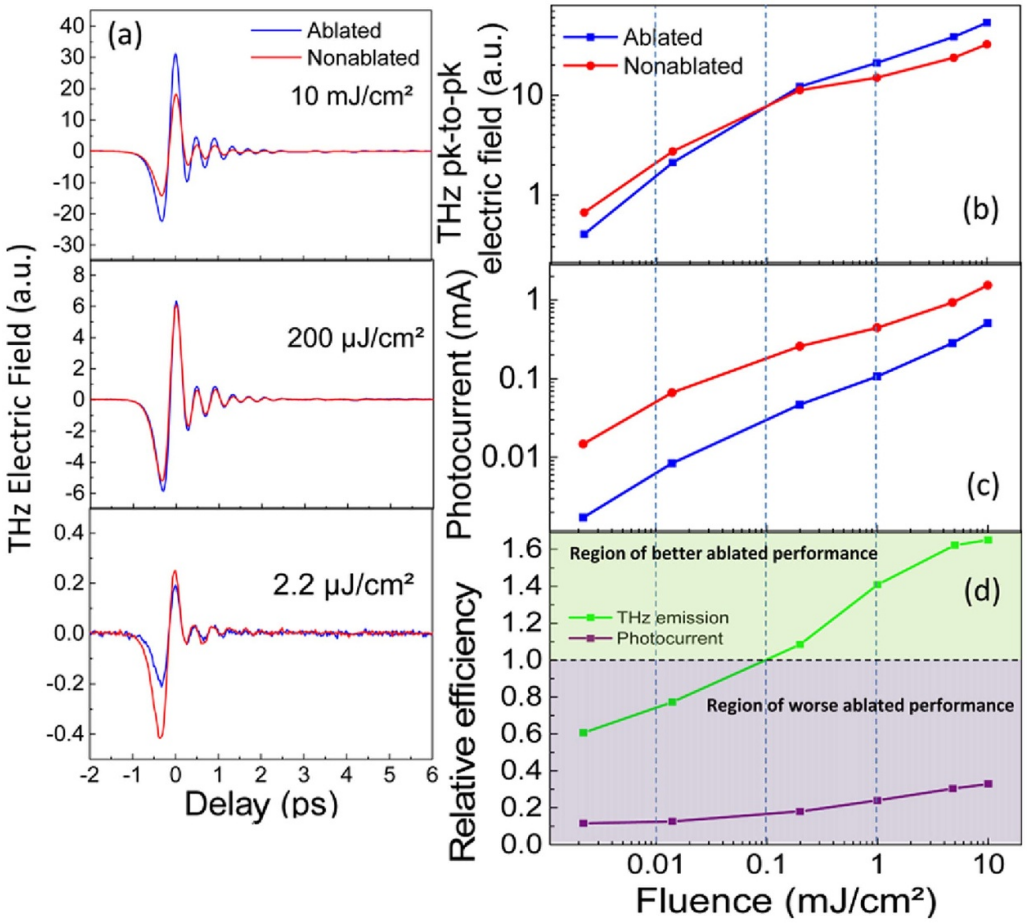


Figure 15. Terahertz (THz)-generated transients obtained for three different optical excitations (2.2 μJ cm^{-2}, 200 μJ cm^{-2}, and 10 mJ cm^{-2}) from the ablated device (blue) and the nonablated device (red). (b) THz peak-to-peak electric field amplitude extracted from (a). (c) Photocurrent versus optical fluence. (d) Comparison of the THz emission (green) and photocurrent (purple) relative efficiency calculated as the ratio between the ablated and nonablated devices from (b) and (c). Reprinted with permission from [169]. © The Optical Society.

4. Antenna designs

Other than the active and substrate material, the main attribute which dictates the functionality and characteristics of a PC emitter is the antenna design. A list of antenna structures is provided in table 2, along with their relative advantages and disadvantages.

4.1. Single gap electrode design

In 1997, Tani *et al* [1] published a comprehensive comparison of three commonly used antenna designs, the Hertzian dipole, the bowtie and the stripline, all with relatively small gap widths of between 5 and 30 μm. These are depicted in figure 16. For small apertures of <100 μm, comparable with the radiation wavelength, the spectral response is dependent on the electrode structure as they filter and direct the beam [87]. Each design was tested on both LT-GaAs and SI-GaAs substrates. Firstly, it is determined that the amplitude of the emitted THz signal/output power was proportional to the length of the dipole antenna (c), which is attributed to a rise in resonant frequency with decreasing electrode length.

Next, it was shown that the spectral bandwidth and peak signal is design dependent, with the stripline antenna producing a THz bandwidth of up to 4 THz with a peak around 1 THz. This is significantly higher than that of dipole and bowtie designs, with values of 3/0.6 THz and 1/0.1 THz for the bandwidth/peak signal, respectively. However, despite the bowtie exhibiting the smallest spectral width, it proves far superior in THz output power, four (six) times that achieved with the stripline (dipole) design under the same excitation conditions [1]. It was also shown with the dipole design that longer lifetime carriers in the SI-GaAs result in a smaller second peak in the THz time-domain waveform and a slightly lower bandwidth than that of the comparative LT-GaAs-based device. This work also touches on one of the main limitations of PC emission which is output saturation due to screening of the bias field by excited photocarriers [180, 181]. This is said to be more influential in the dipole design, owing to the higher optical fluence within the small gap. It also appears to occur at a lower optical power for SI-GaAs devices, compared with LT-GaAs. While no explanation is provided here, Winnerl *et al* [117] suggested that this could be due to the significantly higher carrier mobility in SI-GaAs.

Table 2. Summary of the advantages and disadvantages of the antenna designs discussed within this section.

Design	Advantage	Disadvantage
Bowtie/dipole/slot	Easy to fabricate. High bandwidth output of >4 THz (slot) [1] and dipole designs (>60 THz) [171]. Bowtie exhibits the highest output power [1].	Suffers more from carrier screening (dipole), exhibits a low frequency response (bowtie) [1].
Offset dipole	Generated a singular electric field enhancement resulting in higher THz fields [172].	THz radiation is generated in a perpendicular direction [172].
Circular	Shifts the THz spectrum to a higher frequency [87].	No electric field enhancement due to a lack of sharp points or edges.
Interdigitated array	Utilise higher optical powers than a signal element and can be used to generate high fields [101, 173, 174].	Require slightly more complicated design and fabrication techniques.
Plasmonic nanoelectrodes (see below)	Record efficiencies for PC emitters of 7.5% [175, 176]. High power output 3.8 mW [177].	Saturates at low optical powers, very difficult to fabricate over large areas.
Small gaps (<50 μm)	Broad spectral response, requires a smaller bias voltage to drive device [1, 75].	Large THz diffraction angle, susceptible to carrier screening of the bias field. Can increase fabrication and optical alignment difficulties.
Semi-large gaps (50 μm–1 mm)	Utilise high optical powers (1–3 W). Efficient as they suffer less from screening effects [87, 102, 107]. Easy to fabricate and align in a TDS system.	Saturates under intensity optical illumination from an amplified laser.
Large gaps (>1 mm)	Can generate THz fields exceeding 100 kV cm^{-1} using amplified laser systems [178, 179].	Required high voltage bias source, which can be expensive and can be a source of noise.

A similar study was conducted by Stone *et al* [87] in 2004, who compared bowtie, circular and square electrode designs with semi-large gaps, again on both SI-GaAs and LT-GaAs wafers. Semi-large structures, roughly categorised as those with gaps between 50 μm and 1 mm wide, offer a good compromise in properties and performance [2]. While smaller gaps tend to saturate at low optical powers due to increased Coulomb screening effects [47], larger gaps with active areas over 1 cm^2, require amplified laser systems to excite, significantly higher bias voltages and suffer from other forms of saturation [70, 180]. Semi-large gaps require simple fabrication techniques and can allow full utilisation of high-repetition-rate mode-locked Ti:sapphire lasers. They have also been found to be more efficient than smaller gaps owing to the reduced screening effects [76, 107]. In [87] voltages as high as 350 V and optical powers of 1.1 W where applied to gaps ranging from 0.1 to 2 mm wide. It is shown that smaller aperture devices, especially those with pointed structures (bowtie), give rise to a broader spectral response, an attribute that has been confirmed and utilised by other groups [40, 182]. Furthermore, the circular structure with rounded edges tends to shift the spectrum to higher frequencies without broadening, while the square design demonstrated the narrowest frequency response of all devices. Cai *et al* [172] investigated the use of a dipole design with pointed triangular contacts employing a lateral offset between the contact ends (figure 16). Sharp electrode ends lead to a singular electric field enhancement, resulting in a rise in THz output due an increase in carrier acceleration. Along with device resistivity, this effect is increased when a lateral offset is applied to the electrode ends, as it allows one to maximise the overlap between the high electric fields and the laser excitation spot. Using an LT-GaAs-mounted structure with a 5 μm wide gap and 5 μm lateral tip offset, bias fields as high as 120 kV cm^{-1} can be sustained and used to generate 2.7 μW of THz power. However, a diagonal electric bias field results in 25% of the generated THz radiation in the orthogonal component.

4.2. Metallization and electrode dimensions

Other groups have also investigated the effect of contact metallization on the characteristics of THz antennas [183, 184]. In the former study, Ti/Au was directly compared to AuGe-based alloys, two of the most popular choices for use with GaAs devices. This study suggests that while Ti/Au provides the highest thermal stability owing to the higher melting points of the metals, AuGe contacts provide a reduced impedance due to high diffusion depth of Ge (200 nm) into the LT-GaAs.

This results in high photocurrent and 50% increase in output power over Ti/Au. A similar study conducted by Shi *et al* [107] compares the performance of identical emitters with AuGeNi and Ti/Au electrodes. Ni is added to the metallization to reduce surface oxides and improve wettability. This shows that AuGeNi contacts provide the antenna with a higher breakdown voltage owing to the Schottky contact created between Ti/Au and the active material which generates heat. This also decreases the stability of the device. The same study also reveals that the contact size of a stripline antenna has a significant effect on the device characteristics. Shown in figure 17, a decrease in this width (b) from 80 to 10 μm (with an 80 μm gap) on a stripline antenna results in a drop in THz amplitude of greater than 50%, as well as a significant loss of stability. This is due to higher average temperature at the PC gap, as smaller contacts fail to remove as much heat from active material reducing the carrier mobility of the

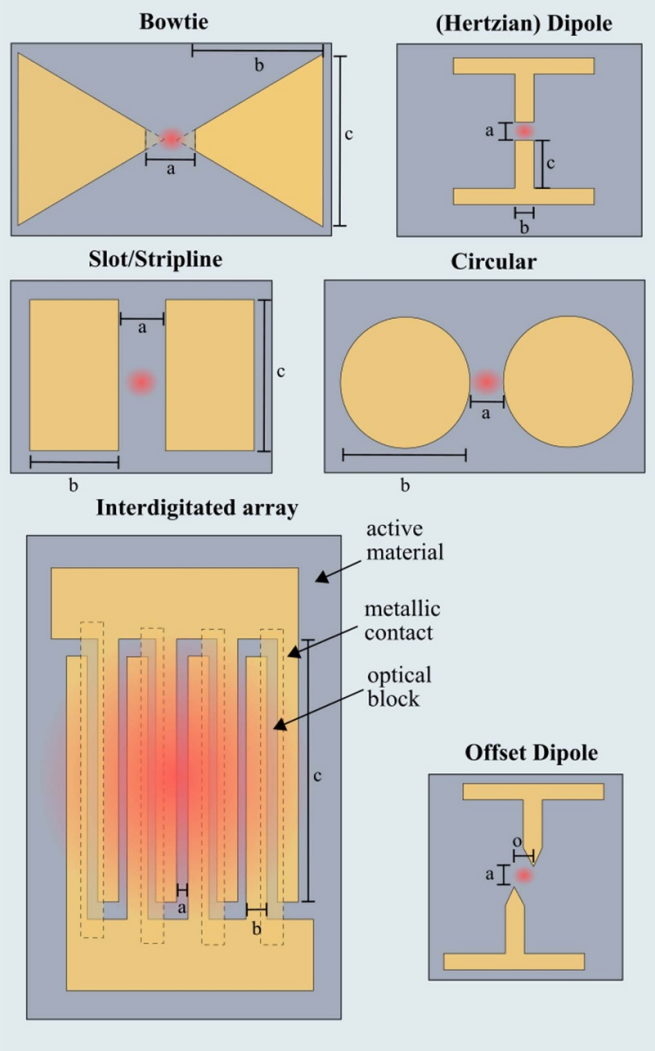


Figure 16. Examples of the commonly used PCA designs. The bowtie design is applied with or without pointed ends. Length a, b, c and o refer to the photoconductive gap, electrode width, length and offset respectively. The red spot represents where the antenna is typically illuminated.

sample. This effect has been confirmed through other studies [185, 186].

4.3. Interdigitated electrode structures

As previously mentioned, there are several factors which limit the THz output power from small gap PC emitters. These include optically induced heating, which reduces carrier mobility and contributes to material breakdown [107], and saturation caused by Coulomb screening [47, 181]. To overcome these limitations and utilize higher powers available from laser sources, a unique interdigitated array design was first proposed by Yoneda *et al* [103]. This geometry, once again depicted in figure 16, typically consists of a single anode and cathode, each connected to multiple parallel interlaced electrodes. By illuminating every other electrode gap to avoid destructive interference, the overall generated THz pulse can be viewed as the constructive addition of the response of each element in

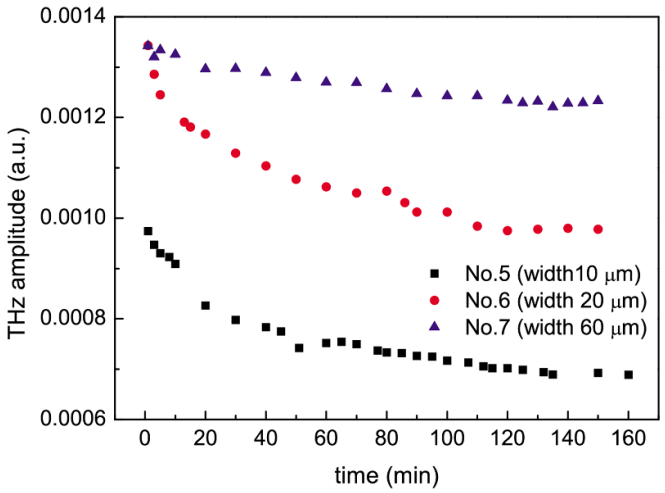


Figure 17. Stability of antennas 5, 6, and 7 with same gap (80 μm and different electrode widths (10, 20, and 80 μm)). The bias voltage of the three antennas changed at the scope of 60–65 V because the resistance of the antennas changed with the temperature. Reprinted with permission from [107]. © The Optical Society.

the array. An advantage to this design, compared with smaller individual gaps, is that a Si lens is not required to collect the outputted radiation as THz diffraction is reduced.

In 2005, this metal–semiconductor–metal geometry was employed by Dreyhaupt *et al* [173] to fabricate a 70 × 70 μm^2 SI-GaAs-mounted array structure, containing finger electrode width and spacing of 5 μm. To avoid deconstructive interference, i.e. to ensure all electrons are accelerated unidirectionally, a second metallization layer was applied above every other gap, on top of an electrically isolating SiO_2 layer. Through flood illumination of the entire array with 200 mW and biasing at a field of 120 kV cm^{-1}, this device demonstrated an output THz field of 85 V cm^{-1} with a bandwidth extending up to 3 THz. However, a drawback of this structure is that only 25% of the incident optical power contributes to generate THz radiation, owing to the low filling factor and reflection losses. Within this study it was also shown that the shorter the electrical pulse duration used to bias the device, the greater the field which can be safely applied before reaching carrier velocity saturation or damaging the material. This is due to a higher duty cycle resulting in a higher substrate temperature, reducing the carrier mobility. This design was adapted by Awad *et al* [101] who used a 1.4 μm thick LT-GaAs layer epitaxially transferred onto a 500 μm thick sapphire substrate. The array itself consisted of 14 individual elements, each with a 11 μm wide PC gap. The LT-GaAs within the 4 μm wide inverted gap (where electrons accelerated in the opposite direction) was etched away, preventing the requirement for a second metallization step and reducing dark current. However, despite this, the maximum fluence which could be sustained was 2.8 × 10^{-3} mW μm^{-2} (350 mW), three-orders-of-magnitude below what was required to saturate a single element.

To improve the efficiency of these array structures, a unique illumination technique was proposed by Matthaus *et al*

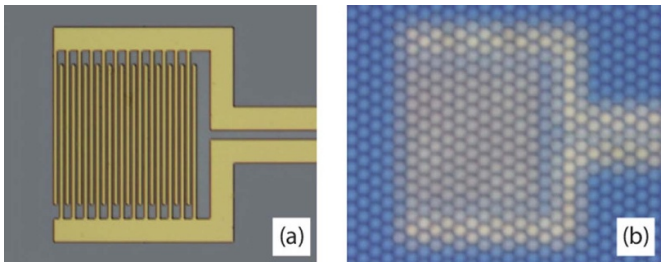


Figure 18. Photo of the large-area emitter without (a) and with hexagonal lens array (b). Reproduced from [174], with the permission of AIP Publishing (DOI: 10.1063/1.2976162).

[174, 187]. Rather than illuminating the entire structure, a microlens array was employed to focus the optical beam onto every other element in the array. The 300 × 300 μm^2 structure, pictured in figure 18, with (b) and without (a) microlens, was fabricated using LT-GaAs-on-SI-GaAs, with electrode and gap widths of 8 and 5 μm, respectively. The average THz power is plotted in figure 19 as a function of bias voltage (upper—normalised) and incident optical power (lower). While the bias control shows the expected quadratic dependence over THz power, the device clearly begins to saturate at high optical fluence. A peak efficiency of 1.35 × 10^{-5} was achieved when applying 200–300 mW of optical power. Furthermore, when using the maximum power available, 540 mW, a THz output power of 6.5 μW was recorded. However, a potential drawback to this technique, compared with flood illumination, is the challenging and time-consuming alignment of the microlens and the array structure, which can be achieved either in the fabrication process or aligned *in-situ* when testing. For this reason, there are few other examples of it being applied [188–190].

Since then, various improvements have been suggested to both the active material [117] and the geometric structure [185, 191] to aide efficiency [192] and bandwidth [75]. For instance, Hale *et al* demonstrated a bandwidth of 20 THz by illuminating an SI-GaAs-mounted array with 3 μm wide PC gaps, with a 15 fs long optical pulse. Employing a bias voltage of 85 V, a calculated peak THz field of 1 kV cm^{-1} was achieved, substantially higher than any previously published array structures with a Ti-sapphire oscillator system. Much of the improved bandwidth is believed to be a result of employing a small PC gap as it results in faster screening of the applied electric field. However, it should be noted that the short optical pulse employed here has a significant effect [193]. A study by Madéo *et al* [194] showed that for these array structures, the frequency of the spectral peak is inversely proportional to the PC gap width. The results from this study are plotted in figure 20.

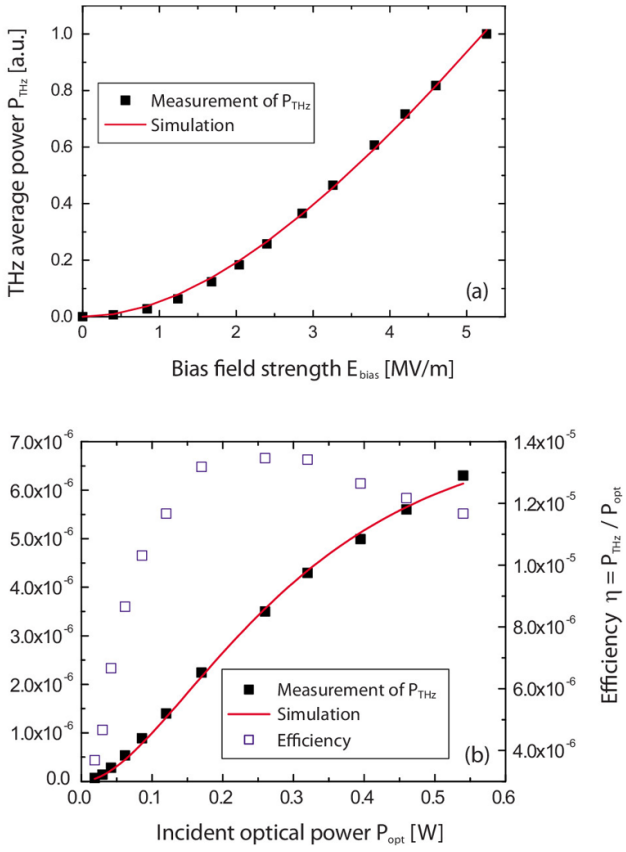


Figure 19. Terahertz average power dependency for (upper) increasing bias field strength and (lower) increasing incident optical power with E_{bias} = 5 V m^{-1}. Reproduced from [174], with the permission of AIP Publishing (DOI: 10.1063/1.2976162).

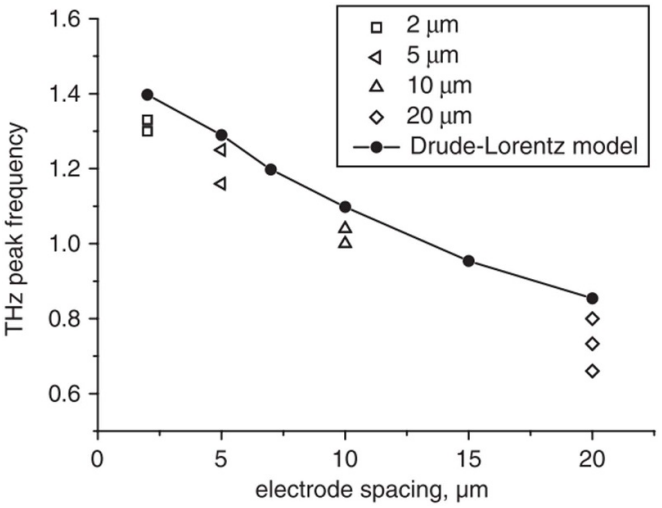


Figure 20. Comparison between measured (open shapes) and simulated (filled circles) peak spectral frequency of different antennas (reprint of figure 3 from [194]). Reproduced with permission from [194].

4.4. Radial and azimuthal polarization antennas

Other unique antenna designs include those with four-contacts, to generate THz radiation whose polarization is alternately switched between two orthogonal directions [195], and those which produce radial or azimuthally polarized radiation [196, 197]. Examples of these are shown in figure 21.

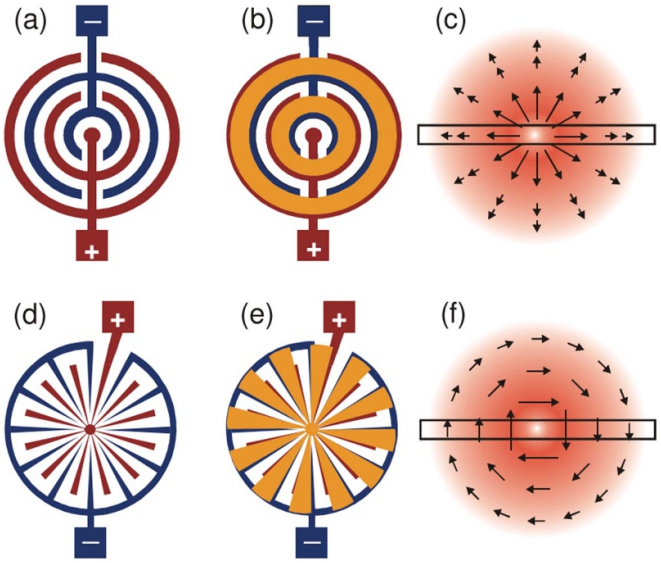


Figure 21. Sketch of electrode geometry (a), (d), full emitter structure (b), (e) with second metallization layer (orange) and resulting mode pattern (c), (f) for radial (a)–(c) and azimuthal (d)–(f) polarization. The arrows in the patterns indicate the electric field direction. Reprinted with permission from [196].
© The Optical Society.

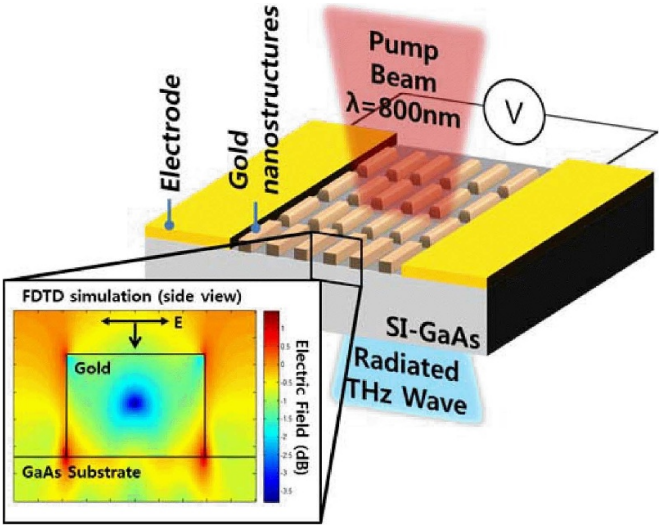


Figure 22. Schematic of the nanoplasmonic THz PCA. Plasmonic nanoantennas are integrated on the photoconductive region. The nanoantennas concentrate the light in near field around nanoantennas. (Reprint of figure 1 from [198]). © 2011 IEEE. Reprinted, with permission, from [198].

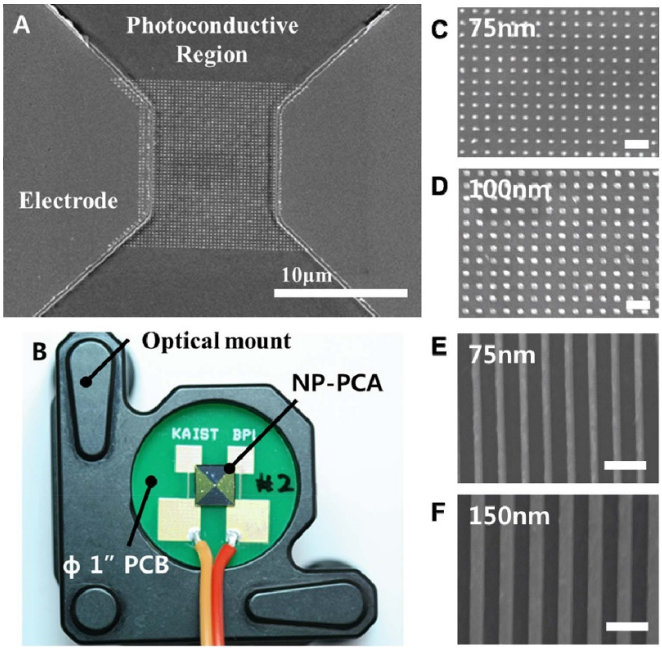


Figure 23. (a) SEM images of nanoplasmonic PCA and plasmonic nanoantennas. (b) Packaged nanoplasmonic PCA on 1″ PCB. Scale bar on bottom SEM images is 500 nm. (c), (d) Nanosquare antennas with two different widths. (e), (f) Nanorod antennas with two different widths. (Reprint of figure 3 from [198]). © 2011 IEEE. Reprinted, with permission, from [198].

4.5. Comparison of the electrode geometries

The key electrode geometries discussed in this section are summarised in table 2.

5. Antenna operation enhancement with plasmonic nanostructures

One of the most substantial and high-profile developments in PC emission in the past ten years has been the emergence of plasmonic nanostructures [175]. These are known to increase light absorption and reduce the average photocarrier transport pathlength, resulting in a faster recapture of carriers on a sub-picosecond timescale. Several groups have demonstrated that this can yield a significant increase in quantum and conversion efficiency over conventional PC emitters [175–177, 189, 198–202].

The first demonstration of a PCA fabricated with metal nanostructures was in 2011 by Park *et al* [198]. In this work, a metallic plasmonic nanostructure is patterned using e-beam lithography between the contacts of a 10 μm wide bowtie antenna, all on top of an SI-GaAs substrate. Schematic and SEM images of this antenna are shown in figures 22 and 23(a) respectively.

Importantly, the resonant wavelength of the plasmonic structure ($\lambda/4$) was designed to match that of the 800 nm pump-pulse, resulting in the excitation of a localised surface plasmon at the metal–semiconductor interface. As this plasmonic wave is tightly confined to this boundary so is the optical absorption, resulting in enhanced localised electric field and a rise in photocarriers near the nanostructure. This contributes to a significant improvement in coupling efficiency and transient-photocurrent, as more of the carriers are collected by the electrode [198]. This effect is only believed to occur when the parallel wave vector of the incident electromagnetic wave matches the surface plasmon wave vector, which can be determined from the metal and dielectric permittivity values [203]. It has been suggested that the locally enhanced bias field is the dominant factor contributing to this effect [204], while

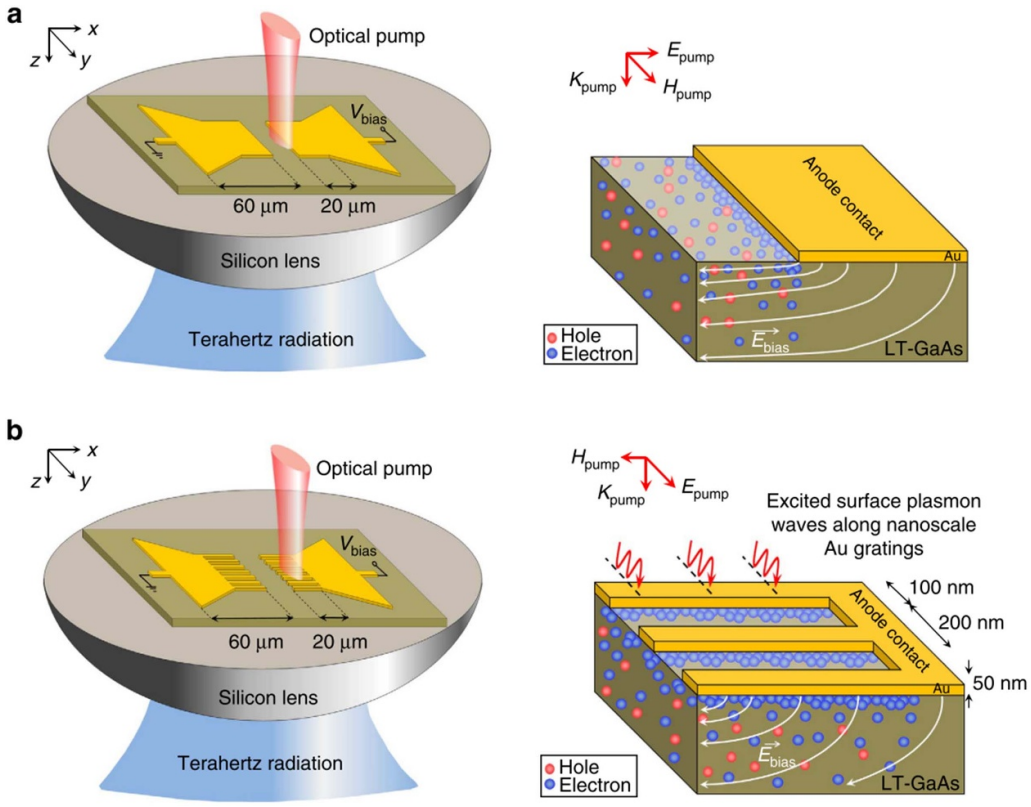


Figure 24. Schematic diagram and operation concept of photoconductive terahertz emitters and detectors. The two bowtie designs with (b) and without (a) nanostructures. (Reprint of figure 1 from [175]). Reprinted by permission from Springer Nature Customer Service Centre GmbH: Springer Nature, Nature Communications [175], Copyright © 2013, Nature Publishing Group, a division of Macmillan Publishers Limited. All Rights Reserved.

asymmetric scattering of the incident photons is also believed to help confine the beam onto the active material [199]. With several different structures tested in this study (figures 23(c) and (f)), a design with 75 nm wide vertically aligned nanorods (E) provided 32% higher output field than an unadopted bowtie design. In later work [199], four variations of this design were tested with increasing nanorod width from 150 to 225 nm, shifting the plasmon resonance of the structure from 735 to 877 nm, respectively. The highest spectral enhancement factor (an average of 2.4 times relative to a reference bowtie design) was shown to occur at a width of 200 nm. This effect is due to matching the resonance of the surface plasmon and pump wavelengths.

In 2013, Berry *et al* [175] introduced a unique design incorporating 20 μm long plasmonic contact electrodes onto the ends of bowtie shaped contact pads. Contrary to [199], here, the horizontally aligned nanostructures are electrically connected to the contacts and a 20 μm wide gap is left between the anode and cathode. Furthermore, this study was conducted using LT-GaAs as the active material and each nanostructure was 100 nm wide (200 nm pitch) and 50 nm high. Figure 24 shows schematic images of the two bowtie designs with (b) and without (a) nanostructures. When illuminated with an 800 nm pump pulse surface plasmon waves are excited along the periodically metallic grating. This in-turn allows transmission of a large portion of the optical power to be absorbed into the active material, especially in close proximity to the electrodes which significantly reduces the carrier transport path to the metal. These combined factors resulted in a 50-fold increase in THz output power, compared with a conventional device. The primary results from this experiment are shown in figures 25(b) and (e). Interestingly, in this regime, the THz output power appears to be linear with photocurrent. This is contrary to many other studies applying larger geometry structures, where saturation effects [47] and optically induced heating [107] complicate the relationship.

To utilise higher optical pump power, this original design has later been adapted yielding output powers of 1.9 [189] and 3.8 mW [177] by incorporating large-area logarithmic spiral and interdigitated array structures, respectively. In [177], the plasmonic nanoelectrodes (same dimensions as [175]) are fabricated overlapping the anode of a interdigitated array structure on an GaAs substrate. When optically excited with 240 mW, this 1×1 mm^2 design yields an order of magnitude higher optical-to-THz conversion efficiency compared with a design with no nanoelectrodes, as well an output of 3.8 mW. Recently published works have concentrated on the use of nanostructured antennas operating at a telecommunication wavelength of 1550 nm [205, 206] and the study of different active materials [207]. For instance, Jooshesh *et al* [205] demonstrated the benefits of below-bandgap excitation of a plasmon-enhanced emitter fabricated on LT-GaAs, over InGaAs which

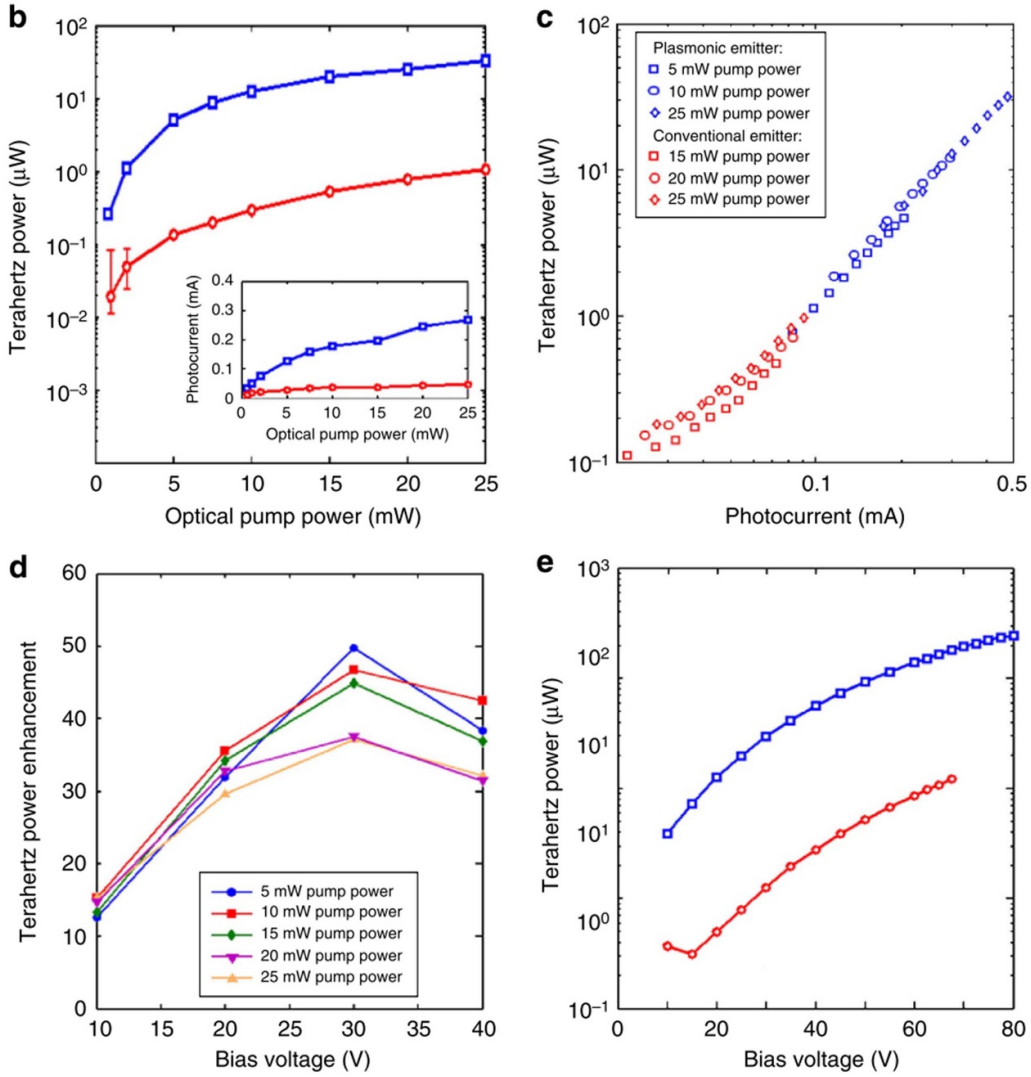


Figure 25. Comparison of the conventional (red) and plasmonic photoconductive terahertz emitter prototypes (blue). (b) (c) and (e) show the output THz power plotted as a function of optical power, photocurrent and bias voltage respectively, while (d) is the calculated enhancement factor over the conventional bowtie antenna. (Reprint of figure 3 from [175]). Reprinted by permission from Springer Nature Customer Service Centre GmbH: Springer Nature, Nature Communications [175], Copyright © 2013, Nature Publishing Group, a division of Macmillan Publishers Limited. All Rights Reserved.

is conventionally used. In this instance the plasmonic structure consists of a slit array with 100 nm gaps and 490 nm pitch length, providing maximum transmission into the substrate for an excitation wavelength of 1570 nm. This device demonstrates more than twice the peak-to-peak output field and bandwidth compared with an InGaAs emitter, which is attributed to the increased optical absorption from midgap states, as well as lower absorption from the gold electrodes at 1550 nm and faster heat dissipation [205]. A similar large-area design as demonstrated in [177] was also presented by Yardimci *et al* [206]. However, in this instance ErAs:InGaAs was chosen as the active material owing to its smaller bandgap. When optical pumped with 400 mW at 1550 nm it generated 300 μW of THz power spread over a bandwidth of 5 THz.

Finally, one of the most exciting designs was presented by Yang *et al* [176] in 2014. This was a unique three-dimensional (3D) nanostructure, consisting of 400 nm tall PC ridges encompassed by a logarithmic spiral antenna for impedance matching [176]. As shown in figure 26(b), the plasmonic metallic grating were fabricated on the sidewalls of these ridges. This allows more carriers to be generated within 100 nm of the anode, resulting in three times higher photocurrent compared with the two-dimensional (2D) structure and contributing more to the efficient generation of the THz pulse [176]. Figures 26(c) and (d) show colour-plots indicating the optical absorption in the 2D and 3D antenna designs respectively. The efficiency is also aided by the addition of a 200 nm thick SiO_2 antireflective coating on the excited surface and a hyper hemispherical silicon lens on the back of the device to improve THz collection. When the design is excited with 1.4 mW of 800 nm pump, a THz output power of 105 μW was recorded, revealing a record-high optical-to-THz conversion efficiencies of 7.5% for PC emission. For a full review of PCAs incorporating nanostructures please read [208, 209].

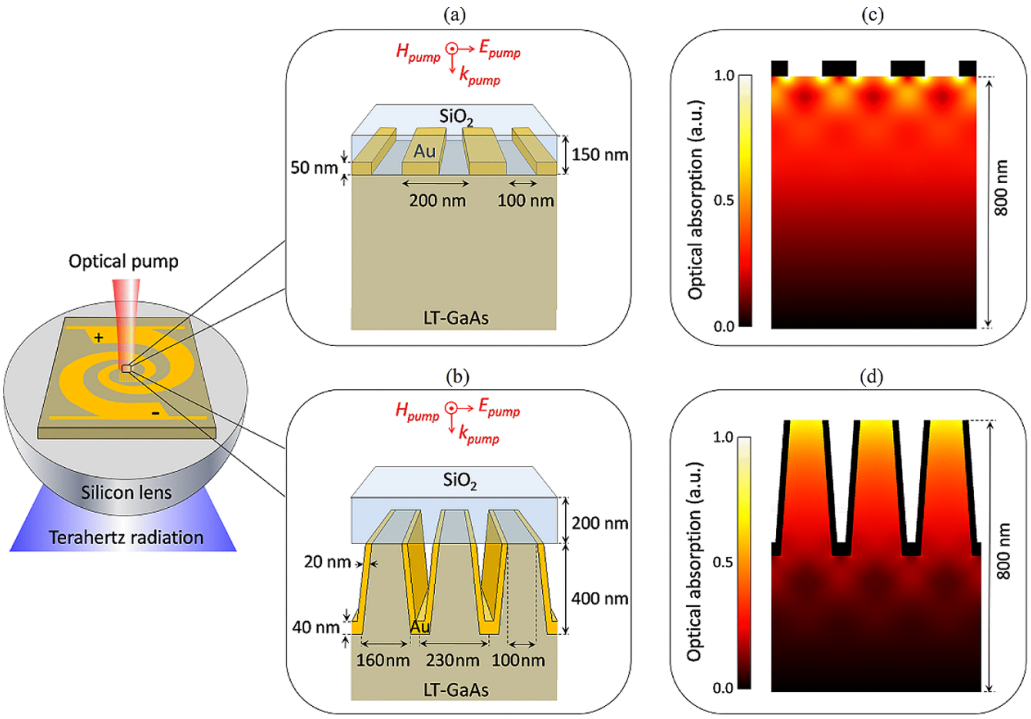


Figure 26. Schematic diagram of plasmonic photoconductive emitters with: (a) two-dimensional plasmonic contact electrodes on the surface of the LT-GaAs substrate and (b) three-dimensional plasmonic contact electrodes embedded inside the LT-GaAs substrate. Colour plot of optical absorption in the LT-GaAs substrate in response to a TM-polarized optical beam at 800 nm wavelength incident on the (c) two-dimensional and (d) three-dimensional plasmonic contact electrodes, respectively. (Reprint of figure 1 from [176]). © 2014 IEEE. Reprinted, with permission, from [176].

6. Large-area PC arrays for high-field THz generation

Over the past ten years, there has been a substantial shift in the community to investigate the use of high-field THz radiation. This has been driven in-part by the increased availability of high-energy table-top amplified laser systems. To reach the high-field regime using PC emission, typically categorized as greater than 100 kV cm^{-1}, historically there are two possible techniques.

6.1. Large-gap GaAs-based PC emitters

The initial approach to increase the saturation threshold and output power was to simply enlarge the size of active area gap [70, 112, 210]. This was first demonstrated by You *et al* [178] in 1992, with a 3.5 cm wide emitter, fabricated on a LT-GaAs-on-SI-GaAs wafer and illuminated with fluences as high as 40 μJ cm^{-2}. Using this approach yielded a peak THz field of 150 kV cm^{-1} which provided the capability to ionise of Rydberg atoms [211] and induce a transient orientation of molecular dipoles in liquids resulting in second-harmonic generation [212]. Following that, in 1996 Budiarto *et al* [179] demonstrated that with a 1 kHz laser system, a 3 cm wide PC gap fabricated on an SI-GaAs wafer is capable of generating peak fields as high as 350 kV cm^{-1}. However, to achieve such THz fields, bias voltages as high as 45 kV over a pulse-width of 2 μs was required. Use of a short electrical pulse width is a technique adopted by several groups, as the low duty cycle reduces heating effects [31, 213]. However, this can lead to significant electrical noise, in addition to the signal noise resulting from the use of a low repetition rate laser system. Another disadvantage to using large-aperture devices is that they are known to suffer more from screening of the bias field by the radiated THz pulse [47, 214]. This issue, combined with the breakdown of material, has restricted the use of PCAs in non-linear high-field experiments. It should be noted that the fabrication of antennas with plasmonic nanostructures over such a large area as required to delay saturation is extremely challenging, limiting its use with amplified laser systems. With these technical difficulties in mind, the most successful approach to date to achieve high-field THz radiation is via array structures.

6.2. GaAs-based array structures

The interdigitated array structure, initially realised by Yoneda *et al* [103], was adapted to work with Ti-sapphire amplified lasers. With the use of a 2 inch diameter SI-GaAs wafer, Harrori *et al* [215] proposed an array structure made from seven individually biased 1 cm^2 units. As can be seen in figure 27, each unit has a single anode and cathode, connected to multiple interlaced parallel electrodes. Despite sustaining bias fields as high as 30 kV cm^{-1}, the quoted saturation fluence of 5 μJ cm^{-2} appeared to limit the potential output of the device to no higher than that of a conventional large-aperture design. Similar designs, consisting of a single array unit on SI-GaAs were later proposed by both Beck *et al* [192] and Winnerl *et al*

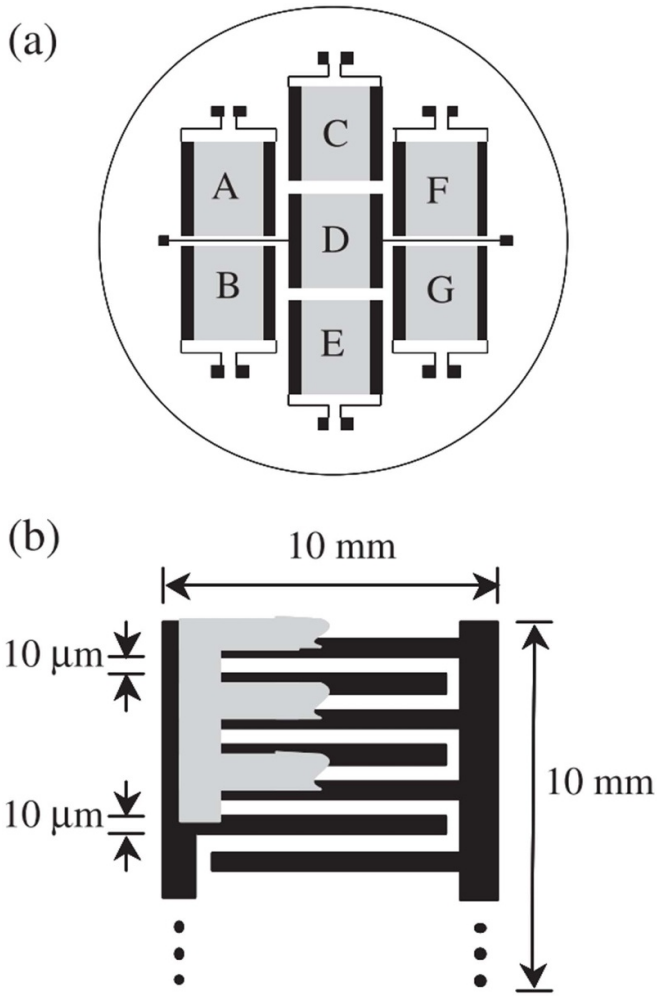


Figure 27. Schematic of THz emitter composed of seven photoconductive antenna units having interdigitated electrode structure. The units are labelled A–G for later reference. (b) Structure of electrodes and shadow mask of each unit. Reproduced from [215]. © IOP Publishing Ltd. All rights reserved.

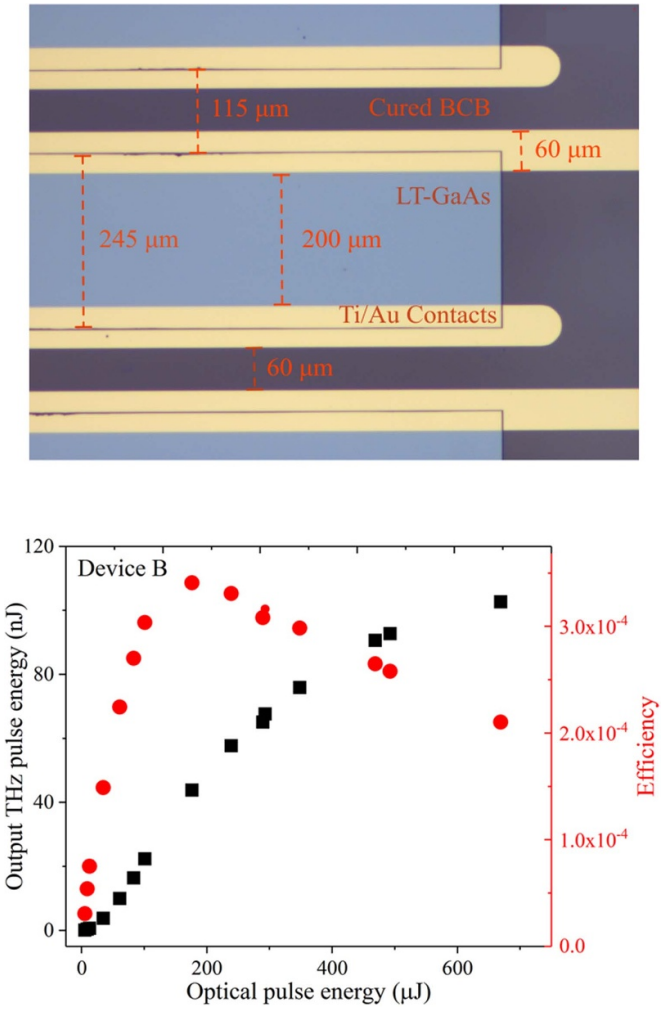


Figure 28. (Upper) microscope image of the sapphire-mounted photoconductive array structure. (Lower) output THz pulse energy (black) and efficiency (red) as a function of optical excitation energy for device B (324 mm^2) when electrically biased at 17.5 kV cm^{-1}. Reprinted with permission from [32]. © The Optical Society. CC BY 4.0.

[35]. In the former, a peak field of 36 kV cm^{-1} was demonstrated by exciting a 1 mm^2 array structure with an optical fluence of 20 μJ cm^{-2} at a repetition rate of 250 kHz. This resulted in a significant improvement in SNR when compared with similar studies [215]. Furthermore the smaller 5 μm wide PC gaps, relative to [215], were able to sustain bias fields as high as 100 kV cm^{-1}, although saturation began at approximately 40 kV cm^{-1}. This also resulted in a superior efficiency over large-aperture devices, owing to the local field enhancement, due in-part to more electrons with higher effective mobility being generated in close proximity to the anode [45, 216, 217]. However, while this proved a step forward for SI-GaAs-based emitters, the low saturation fluence compared with large-aperture devices was still clearly restricting the potential output of array structures.

The saturation fluence of large-gap antennas, F_{sat}, can be written as the following [112]:

$$F_{sat} = \frac{h\upsilon\,(1+n)}{e\mu\eta_O\,(1-R)}. \qquad (3)$$

Here η_O represents the impedance of free-space, R and n are the optical reflectivity of the substrate and its refractive index at submillimetre wavelengths respectively, and $h\upsilon$ and e are the pump photon energy and electron charge. μ represents the mobility of photoexcited carriers, meaning that the saturation fluence is inversely proportional to the carrier mobility, an observation supported by several studies [1, 117]. This suggests that low mobility material could yield a higher output when using high energy excitation.

This approach was recently demonstrated by Bacon *et al* [32] where a 2 μm thick layer of LT-GaAs was bonded directly to an insulating sapphire substrate and used to fabricate a scalable 1.8 cm^2 device with 200 μm wide PC gaps. The semi-large PC gap [107] and electrode width [185] were optimised to ensure a high efficiency and filling factor. An image of this structure is shown in figure 28 (upper), along with the output energy and conversion efficiency as function of optical pulse energy (lower). With a peak excitation pulse energy of

650 μJ focusing through the sapphire substrate, a conversion efficiency of greater than 3×10^{-4} was demonstrated. This led to an output energy 113 nJ and a THz field of 120 kV cm^{-1} by applying a bias field of only 20 kV cm^{-1}, representing a significant improvement in output field for GaAs-based PCA array structure. Much of this improvement is believed to be due to the sapphire substrate acting as a heat sink lowering the average temperature of the LT-GaAs, as well as geometric features of the device optimised for high efficiency. However, despite this, saturation occurs as a function of excitation pulse energy below 650 μJ.

6.3. Wide bandgap-based PCAs

In order to utilize the full capability of table-top laser technology, other wide-band-gap materials such as ZnSe [213, 218] and 6H- [219] and 4H-SiC [220] have been considered. With bandgaps of 2.7 eV (ZnSe), 3.01 eV (6H-SiC) and 3.23 eV (4H-SiC), single-photon excitation requires pumping at 400 nm or shorter, the second harmonic of the 800 nm fundamental beam. Both ZnSe and SiC possess desirable attributes for PC material, with high-dielectric strength compared with SI-GaAs [221], good carrier mobility (>300 cm^2 V^{-1} s^{-1}) [218, 220] and reasonable thermal conductivity. This has led to numerous examples of high-field low-frequency THz generation using ZnSe [31, 213, 222, 223]. In a major step forward in 2016, Ropagnol *et al* demonstrated the ability to reach an output pulse energy of 8.3 μJ using a 12.2 cm^2 array fabricated on a ZnSe substrate. This was illuminated with a pulse energy of 15 mJ at a wavelength of 400 nm [31]. The experimental arrangement used to test this device is depicted in figure 29. To reach such a high output energy, shadow masking was employed on every other gap and a maximum voltage of 7 kV (42 kV cm^{-1}) was applied across each of the 700 μm wide PC gaps. The output pulse energy and conversion efficiency are plotted in figures 30(a) and (b) respectively, both as a function of optical pulse energy at 400 nm. When focusing with a pulse energy of 8.3 μJ, a THz field of 331 kV cm^{-1} was achieved. Interestingly, such a large device has a significant capacitive load, leading to strong distortions and reduction in the temporal profile of the applied electrical pulse. This factor limits the dimensions of the array structure. In later work, the same group also demonstrated the influence of PC gap width on this design, systematically varying it from 400 to 932 μm [223]. Similar to previously published works on different designs [107], they determined that saturation occurs earlier for devices with smaller gaps due to the large capacitance of these arrays, which can be linked to space-charge screening.

Finally, in 2019 Ropagnol *et al* [224] compared the THz response of ZnSe with four different wide bandgap semiconductors, 4H- and 6H-SiC, GaN and Ga_2O_2. As most of these materials have bandgaps greater than 3.1 eV, illuminating at a wavelength of 400 nm would not be sufficient to photoexcite electrons. For this reason, the study is conducted with a hybrid dye-excimer (KrF) laser delivering 500 fs long pulses at 248 nm. Firstly, all materials were tested as function of optical fluence and bias field, when exciting a simple a stripline antenna with a 3 mm wide gap. In both cases, 4H-SiC was identified as the best performing material to produce the highest output power. Next, large-area array structures were fabricated using 4H-SiC and 6H-SiC 4 inch diameter wafers. Each structure had 20 1 mm wide PC gaps but used shadow masking to optical block half of them to ensure constructive interference. Once again, 4H-SiC seemed to be the better performing material with 100% higher output at a bias field of 27 kV cm^{-1}. Using this device, a maximum output THz pulse energy of 11 μJ was recorded with an UV pump of 54 mJ. One disadvantage to using this material is that almost all the outputted radiation is below 500 GHz. This limits the achievable spot-size and the THz field. As such, the maximum THz field was calculated to be 117 kV cm^{-1}.

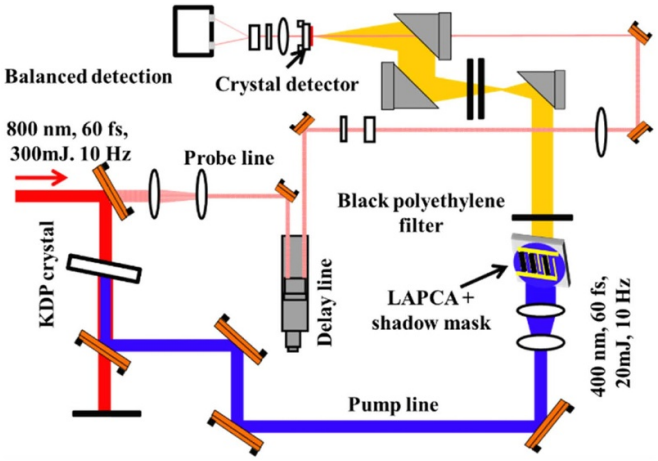


Figure 29. Schematic of the setup for generation of intense THz pulses with an interdigitated ZnSe LAPCA excited at 400 nm. Reprinted with permission from [31]. © The Optical Society.

7. Summary and future challenges

In this article, we have provided an up-to-date review of the broad and well-established topic of pulsed THz radiation through PC emission. In section 3, we have discussed the key advantages and disadvantages of the various materials, optically pumped with a range of excitation wavelengths. In sections 4 and 5 we have examined commonly employed electrode designs and discussed their key attributes, before moving to high-field designs in section 6. The previous 30 years of PCA development has brought about significant improvements in almost every measurable characteristic of the device. It is these incremental advances in efficiency, output power, bandwidth and SNR which has led to the PCA being both commercially viable, and the most popular method of generating short-pulse THz radiation in a compact table-top setting. Other less well-known techniques include active mode-locking and pulse dispersion in THz quantum cascade lasers [225–227] and optical rectification in non-linear crystals [228]. However, they do come with drawbacks such as low conversion efficiency or reduced bandwidth, therefore are not as commonly employed.

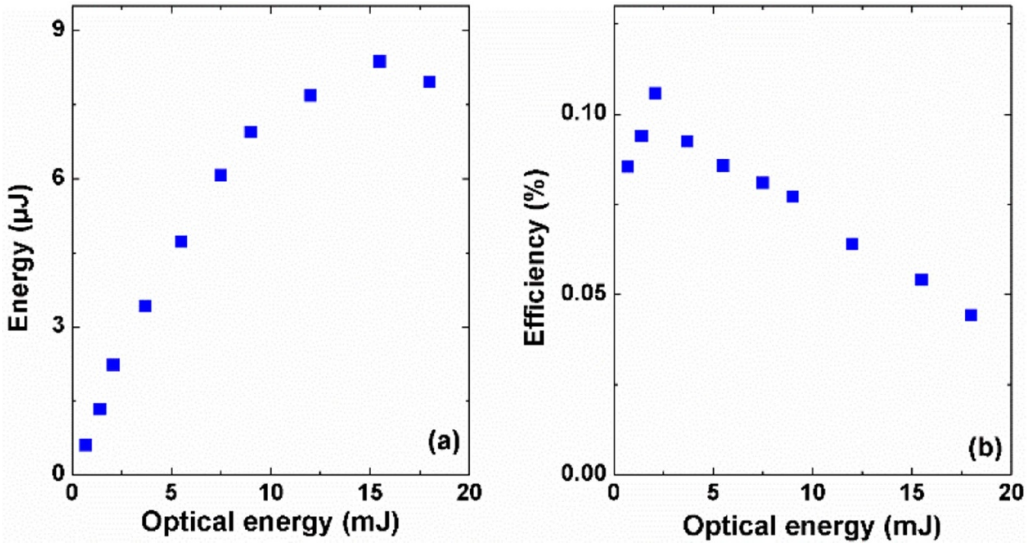


Figure 30. (a) Energy and (b) optical-to-THz conversion efficiency as a function of optical energy for the radiation of THz pulses from interdigitated ZnSe LAPCA with Cr/Au contacts illuminated and biased at 42 kV cm^{-1}. Reprinted with permission from [31]. © The Optical Society.

Despite the success of the PCA there are still many challenges to be resolved, especially regarding the generation of wideband high-field THz radiation. It is here where other methods such as two-colour plasma generation [229] and use of non-linear crystals [230] are the more popular choices. While PC antennas provide direct bias control over the THz field and its polarisation, they also suffer from saturation effects at high optical intensities. It is therefore clear that further innovations in both active materials and electrode designs are required to avoid this. To further develop these devices and improve the commercial viability, there is a clear and conscious shift to longer wavelength excitation. However, there is currently a limited number of materials which work effectively at 1030 nm and are therefore compatible with Yb-doped fibre-lasers [119] or thin-disk lasers [231]. This combination could result in high-average-power THz radiation, important for linear spectroscopy of heavily attenuating materials at high repetition rate.

Data availability statement

No new data were created or analysed in this study.

Acknowledgments

This work was supported by JSPS KAKENHI Grant number 21K14217 and in part by funding from the Femtosecond Spectroscopy Unit, Okinawa Institute of Science and Technology Graduate University. We also would like to acknowledge Lorena Andreoli for her support and Dr Sarah Morson for kindly proofreading the manuscript.

ORCID iD

David R Bacon https://orcid.org/0000-0001-8385-0614

References

[1] Tani M, Matsuura S, Sakai K and Nakashima S 1997 Emission characteristics of photoconductive antennas based on low-temperature-grown GaAs and semi-insulating GaAs *Appl. Opt.* **36** 7853
[2] Shen Y C, Upadhya P C, Beere H E, Linfield E H, Davies A G, Gregory I S, Baker C, Tribe W R and Evans M J 2004 Generation and detection of ultrabroadband terahertz radiation using photoconductive emitters and receivers *Appl. Phys. Lett.* **85** 164–6
[3] Jepsen P U, Jacobsen R H and Keiding S R 1996 Generation and detection of terahertz pulses from biased semiconductor antennas *J. Opt. Soc. Am.* B **13** 2424
[4] Grischkowsky D, Keiding S, van Exter M and Fattinger C 1990 Far-infrared time-domain spectroscopy with terahertz beams of dielectrics and semiconductors *J. Opt. Soc. Am.* B **7** 2006
[5] van Exter M, Fattinger C and Grischkowsky D 1989 Terahertz time-domain spectroscopy of water vapor *Opt. Lett.* **14** 1128–30
[6] Schmuttenmaer C A 2004 Exploring dynamics in the far-infrared with terahertz spectroscopy *Chem. Rev.* **104** 1759–79
[7] Zeitler J A, Taday P F, Newnham D A, Pepper M, Gordon K C and Rades T 2007 Terahertz pulsed spectroscopy and imaging in the pharmaceutical setting—a review *J. Pharm. Pharmacol.* **59** 209–23
[8] Davies A G, Burnett A D, Fan W, Linfield E H and Cunningham J E 2008 Terahertz spectroscopy of explosives and drugs *Mater. Today* **11** 18–26
[9] Appleby R and Wallace H B 2007 Standoff detection of weapons and contraband in the 100 GHz to 1 THz region *IEEE Trans. Antennas Propag.* **55** 2944–56
[10] Woodward R M, Wallace V P, Arnone D D and Linfield E H 2003 Terahertz pulsed imaging of skin cancer in the time and frequency domain *J. Biol. Phys.* **29** 257–61
[11] Ashworth P C, Pickwell-macpherson E, Provenzano E, Pinder S E, Purushotham A D, Pepper M and Wallace V P 2009 Terahertz pulsed spectroscopy of freshly excised human breast cancer *Opt. Express* **17** 93–4

[12] Pickwell-macpherson E and Wallace V P 2017 Biomedical applications of terahertz technology *J. Phys. D: Appl. Phys.* **39** 301–10

[13] Nagai M, Yada H, Arikawa T and Tanaka K 2006 Terahertz time-domain attenuated total reflection spectroscopy in water and biological solution *Int. J. Infrared Millimeter Waves* **27** 505–15

[14] Yada H, Nagai M and Tanaka K 2008 Origin of the fast relaxation component of water and heavy water revealed by terahertz time-domain attenuated total reflection spectroscopy *Chem. Phys. Lett.* **464** 166–70

[15] Yada H, Nagai M and Tanaka K 2009 The intermolecular stretching vibration mode in water isotopes investigated with broadband terahertz time-domain spectroscopy *Chem. Phys. Lett.* **473** 279–83

[16] Zielbauer J and Wegener M 1996 Ultrafast optical pump THz-probe spectroscopy on silicon *Appl. Phys. Lett.* **68** 1223–5

[17] Bae J M *et al* 2017 Ultrafast photocarrier dynamics related to defect states of $Si_{1-x}Ge_x$ nanowires measured by optical pump-THz probe spectroscopy *Nanoscale* **9** 8015–23

[18] Zhong H, Xu J, Xie X U, Yuan T, Reightler R, Madaras E and Zhang X-C 2005 Nondestructive defect identification with terahertz time-of-flight tomography *IEEE Sens.* **5** 203–8

[19] Hirori H and Tanaka K 2016 Dynamical nonlinear interactions of solids with strong terahertz pulses *J. Phys. Soc. Japan* **85** 082001

[20] Hafez H A *et al* 2016 Intense terahertz radiation and their applications *J. Opt.* **18** 9

[21] Bensky T J, Haeffler G and Jones R R 1997 Ionization of Na Rydberg atoms by subpicosecond quarter-cycle circularly polarized pulses *Phys. Rev. Lett.* **79** 2018–21

[22] Li S and Jones R R 2014 Ionization of excited atoms by intense single-cycle THz pulses *Phys. Rev. Lett.* **112** 1–5

[23] Kampfrath T, Tanaka K and Nelson K A 2013 Resonant and nonresonant control over matter and light by intense terahertz transients *Nat. Photon.* **7** 680–90

[24] Yasuda H H Ã, M, Kawai M, Hinode F, Nanbu K and Miyahara F 2011 Intense coherent terahertz generation from accelerator-based sources *Nucl. Instrum. Methods Phys. Res.* A **637** S57–S61

[25] Yeh K-L, Hoffmann M C, Hebling J and Nelson K A 2007 Generation of 10 μJ ultrashort terahertz pulses by optical rectification *Appl. Phys. Lett.* **90** 171121

[26] Hirori H, Doi A, Blanchard F and Tanaka K 2011 Single-cycle terahertz pulses with amplitudes exceeding 1 MV/cm generated by optical rectification in $LiNbO_3$ *Appl. Phys. Lett.* **98** 91106

[27] Meyer F, Vogel T, Ahmed S and Saraceno C J 2020 Single-cycle, MHz repetition rate THz source with 66 mW of average power *Opt. Lett.* **45** 2494

[28] Koulouklidis A D, Gollner C, Shumakova V, Fedorov V Y, Pugžlys A, Baltuška A and Tzortzakis S 2020 Observation of extremely efficient terahertz generation from mid-infrared two-color laser filament *Nat. Commun.* **11** 1–8

[29] Dai J, Xie X and Zhang X-C 2006 Detection of broadband terahertz waves with a laser-induced plasma in gases *Phys. Rev. Lett.* **97** 103903

[30] Cook D J and Hochstrasser R M 2000 Intense terahertz pulses by four-wave rectification in air *Opt. Lett.* **25** 1210–2

[31] Ropagnol X *et al* 2016 Intense THz pulses with large ponderomotive potential generated from large aperture photoconductive antennas *Opt. Express* **44** 83001–45016

[32] Bacon D R, Gill T B, Rosamond M, Burnett A D, Dunn A, Li L, Linfield E H, Davies A G, Dean P and Freeman J R 2020 Photoconductive arrays on insulating substrates for high-field terahertz generation *Opt. Express* **28** 17219–31

[33] Mosley C D W, Staniforth M, Serrano A I H, Pickwell-Macpherson E and Lloyd-Hughes J 2019 Scalable interdigitated photoconductive emitters for the electrical modulation of terahertz beams with arbitrary linear polarization *AIP Adv.* **9** 045323

[34] Burford N M and El-Shenawee M O 2017 Review of terahertz photoconductive antenna technology *Opt. Eng.* **56** 010901

[35] Winnerl S 2012 Scalable microstructured photoconductive terahertz emitters *J. Infrared Millimeter Terahertz Waves* **33** 431–54

[36] Castro-Camus E and Alfaro M 2016 Photoconductive devices for terahertz pulsed spectroscopy: a review [Invited] *Photon. Res.* **4** A36–A42

[37] Fattinger C and Grischkowsky D 1989 Terahertz beams *Appl. Phys. Lett.* **54** 490–2

[38] Lee Y S 2009 *Principles of terahertz science and technology* (Springer) 1–340

[39] Tani M, Sakai K and Mimura H 1997 Ultrafast photoconductive detectors based on semi-insulating GaAs and InP *Japan. J. Appl. Phys.* 2 **36** 9A

[40] Kono S, Tani M, Gu P and Sakai K 2000 Detection of up to 20 THz with a low-temperature-grown GaAs photoconductive antenna gated with 15 fs light pulses *Appl. Phys. Lett.* **77** 4104–6

[41] Wu Q and Zhang X C 1995 Free-space electro-optic sampling of terahertz beams *Appl. Phys. Lett.* **67** 3523

[42] Auston D H, Johnson A M, Smith P R and Bean J C 1980 Picosecond optoelectronic detection, sampling, and correlation measurements in amorphous semiconductors *Appl. Phys. Lett.* **37** 371–3

[43] Auston D H 1983 Subpicosecond electro-optic shock waves *Appl. Phys. Lett.* **43** 713–5

[44] Auston D H, Cheung K P and Smith P R 1984 Picosecond photoconducting Hertzian dipoles *Appl. Phys. Lett.* **45** 284–6

[45] Katzenellenbogen N and Grischkowsky D 1991 Efficient generation of 380 fs pulses of THz radiation by ultrafast laser pulse excitation of a biased metal-semiconductor interface *Appl. Phys. Lett.* **58** 222–4

[46] Kamo Y, Kitazawa S, Ohshima S and Hosoda Y 2014 Highly efficient photoconductive antennas using optimum low-temperature-grown GaAs layers and Si substrates *Japan. J. Appl. Phys.* **53** 3

[47] Rodriguez G and Taylor A J 1996 Screening of the bias field in terahertz generation from photoconductors *Opt. Lett.* **21** 1046–8

[48] Singh A, Pal S, Surdi H, Prabhu S S, Nanal V and Pillay R G 2014 Highly efficient and electrically robust carbon irradiated semi-insulating GaAs based photoconductive terahertz emitters *Appl. Phys. Lett.* **104** 063501

[49] Murotani T, Shimanoe T and Mitsui S 1978 Growth temperature dependence in molecular beam epitaxy of gallium arsenide *J. Cryst. Growth* **45** 302–8

[50] Gregory I S, Baker C, Tribe W R, Evans M J, Beere H E, Linfield E H, Davies A G and Missous M 2003 High resistivity annealed low-temperature GaAs with 100 fs lifetimes *Appl. Phys. Lett.* **83** 4199–201

[51] Luo J K, Thomas H, Morgan D V, Westwood D and Williams R H 1994 The electrical breakdown properties of GaAs layers grown by molecular beam epitaxy at low temperature *Semicond. Sci. Technol.* **9** 2199–204

[52] Salem B, Morris D, Aimez V, Beerens J, Beauvais J and Houde D 2005 Pulsed photoconductive antenna terahertz sources made on ion-implanted GaAs substrates *J. Phys.: Condens. Matter* **17** 7327–33

[53] Liu T-A, Tani M and Pan C-L 2003 THz radiation emission properties of multienergy arsenic-ion-implanted GaAs and

semi-insulating GaAs based photoconductive antennas *J. Appl. Phys.* **93** 2996–3001
[54] Pacebutas V, Biciunas A, Balakauskas S, Krotkus A and Andriukaitis G 2010 Terahertz time-domain-spectroscopy system based on femtosecond Yb:fiberlaser and GaBiAs photoconducting components *Appl. Phys. Lett.* **97** 1–4
[55] Leyman R R, Gorodetsky A, Bazieva N, Molis G, Krotkus A, Clarke E and Rafailov E U 2016 Quantum dot materials for terahertz generation applications *Laser Photonics Rev.* **10** 772–9
[56] Gorodetsky A, Bazieva N and Rafailov E U 2016 Quantum-dot based ultrafast photoconductive antennae for efficient THz radiation Proceedings Volume 9737, Synthesis and Photonics of Nanoscale Materials XIII; 97370C (*San Francisco, California, United States*) **9737**
[57] Singh A, Pashkin A, Winnerl S, Welsch M, Beckh C, Sulzer P, Leitenstorfer A, Helm M and Schneider H 2020 Up to 70 THz bandwidth from an implanted Ge photoconductive antenna excited by a femtosecond Er:fibrelaser *Light Sci. Appl.* **9** 30
[58] Pearton S J, Abernathy C R, Panish M B, Hamm R A and Lunardi L M 1989 Implant-induced high-resistivity regions in InP and InGaAs *J. Appl. Phys.* **66** 656–62
[59] Mohandas R A *et al* 2016 Generation of continuous wave terahertz frequency radiation from metal-organic chemical vapour deposition grown Fe-doped InGaAs and InGaAsP *J. Appl. Phys.* **119** 1–7
[60] Sengupta S, Wilke I and Dutta P S 2009 Ultrafast carrier mobilities in high-resistivity iron-doped Ga 0.69In0.31As photoconducting antennas *Appl. Phys. Lett.* **95** 2007–10
[61] Kohlhaas R B, Breuer S, Liebermeister L, Nellen S, Deumer M, Schell M, Semtsiv M P, Masselink W T and Globisch B 2020 637 μW emitted terahertz power from photoconductive antennas based on rhodium doped InGaAs *Appl. Phys. Lett.* **117** 3–7
[62] Dietz R J B, Globisch B, Gerhard M, Velauthapillai A, Stanze D, Roehle H, Koch M, Göbel T and Schell M 2013 64 μW pulsed terahertz emission from growth optimized InGaAs/InAlAs heterostructures with separated photoconductive and trapping regions *Appl. Phys. Lett.* **103** 1–5
[63] Kostakis I, Saeedkia D and Missous M 2012 Terahertz generation and detection using low temperature grown InGaAs-InAlAs photoconductive antennas at 1.55 μm pulse excitation *IEEE Trans. Terahertz Sci. Technol.* **2** 617–22
[64] O'Hara J F, Zide J M O, Gossard A C, Taylor A J and Averitt R D 2006 Enhanced terahertz detection via ErAs:GaAs nanoisland superlattices *Appl. Phys. Lett.* **88** 1–4
[65] Ospald F, Maryenko D, von Klitzing K, Driscoll D C, Hanson M P, Lu H, Gossard A C and Smet J H 2008 1.55 μm ultrafast photoconductive switches based on ErAs:InGaAs *Appl. Phys. Lett.* **92** 131117
[66] Zhang W, Brown E R, Mingardi A, Mirin R P, Jahed N and Saeedkia D 2019 THz superradiance from a GaAs:ErAs quantum dot array at room temperature *Appl. Sci.* **9** 15
[67] Nandi U, Mohammadi M, Norman J, Grossard A C, Alff L and Preu S 2021 Material properties and performance of ErAs:In(Al)GaAs photoconductors for 1550 nm laser operation *J. Vac. Sci. Technol.* A **39** 1–9
[68] van Exter M, Fattinger C and Grischkowsky D 1989 High-brightness terahertz beams characterized with an ultrafast detector *Appl. Phys. Lett.* **55** 337–9
[69] Smith P R, Auston D H and Nuss M C 1988 Subpicosecond photoconducting dipole antennas *IEEE J. Quantum Electron.* **24** 255–60
[70] Hu B B, Darrow J T, Zhang X C, Auston D H and Smith P R 1990 Optically steerable photoconducting antennas *Appl. Phys. Lett.* **56** 886–8
[71] Warren A C, Katzenellenbogen N, Grischkowsky D, Woodall J M, Melloch M R and Otsuka N 1991 Subpicosecond, freely propagating electromagnetic pulse generation and detection using GaAs:As epilayers *Appl. Phys. Lett.* **58** 1512–4
[72] Tani M, Sakai K, Abe H, Nakashima S-I, Harima H, Hangyo M, Tokuda Y, Kanamoto K, Abe Y and Tsukada N 1994 Spectroscopic characterization of low-temperature grown GaAs epitaxial films *Japan. J. Appl. Phys.* **33** 4807–11
[73] Hu B B, Zhang X C and Auston D H 1990 Temperature dependence of femtosecond electromagnetic radiation from semiconductor surfaces *Appl. Phys. Lett.* **57** 2629–31
[74] Sun F G, Wagoner G A and Zhang X C 1995 Measurement of free-space terahertz pulses via long-lifetime photoconductors *Appl. Phys. Lett.* **67** 1656–8
[75] Hale P J, Madeo J, Chin C, Dhillon S S, Mangeney J, Tignon J and Dani K M 2014 20 THz broadband generation using semi-insulating GaAs interdigitated photoconductive antennas *Opt. Express* **22** 26358
[76] Zhao G, Schouten R N, van der Valk N, Wenckebach W T and Planken P C M 2002 Design and performance of a THz emission and detection setup based on a semi-insulating GaAs emitter *Rev. Sci. Instrum.* **73** 1715–8
[77] Holmes D E, Chen R T, Elliott K R and Kirkpatrick C G 1982 Stoichiometry-controlled compensation in liquid encapsulated Czochralski GaAs *Appl. Phys. Lett.* **40** 46–8
[78] Nuss M C, Auston D H and Capasso F 1987 Direct subpicosecond measurement of carrier mobility of photoexcited electrons in gallium arsenide *Phys. Rev. Lett.* **58** 2355–8
[79] Weiner J S and Yu P Y 1984 Free carrier lifetime in semi-insulating GaAs from time-resolved band-to-band photoluminescence *J. Appl. Phys.* **55** 3889–91
[80] Nelson R J and Sobers R G 1978 Minority-carrier lifetimes and internal quantum efficiency of surface-free GaAs *J. Appl. Phys.* **49** 6103–8
[81] Smith F W, Calawa A R, Chen C L, Manfra M J and Mahoney L J 1988 New MBE buffer used to eliminate backgating in GaAs MESFET's *IEEE Electron Device Lett.* **9** 77–80
[82] Smith F W, Le H Q, Diadiuk V, Hollis M A, Calawa A R, Gupta S, Frankel M, Dykaar D R, Mourou G A and Hsiang T Y 1989 Picosecond GaAs-based photoconductive optoelectronic detectors *Appl. Phys. Lett.* **54** 890–2
[83] Lochtefeld A J, Melloch M R, Chang J C P and Harmon E S 1996 The role of point defects and arsenic precipitates in carrier trapping and recombination in low-temperature grown GaAs *Appl. Phys. Lett.* **69** 1465–7
[84] Gupta S, Frankel M Y, Valdmanis J A, Whitaker J F, Mourou G A, Smith F W and Calawa A R 1991 Subpicosecond carrier lifetime in GaAs grown by molecular beam epitaxy at low temperatures *Appl. Phys. Lett.* **59** 3276–8
[85] Harmon E S, Melloch M R, Woodall J M, Nolte D D, Otsuka N and Chang C L 1993 Carrier lifetime versus anneal in low temperature growth GaAs *Appl. Phys. Lett.* **63** 2248–50
[86] Frankel M Y, Whitaker J F, Mourou G H, Smith F W and Calawa A R 1990 High-voltage picosecond photoconductor switch based on low-temperature-grown GaAs *IEEE Trans. Electron Devices* **37** 2493–8

[87] Stone M R, Naftaly M, Miles R E, Fletcher J R and Steenson D P 2004 Electrical and radiation characteristics of semilarge photoconductive terahertz emitters *IEEE Trans. Microw. Theory Tech.* **52** 2420–9

[88] Stone M R, Naftaly M, Zinov N N and Miles R E 2002 Characteristics of large-aperture photoconductive terahertz antennas *Proceedings, IEEE Tenth International Conference on Terahertz Electronics* 125–8

[89] Look D C 1993 Molecular beam epitaxial GaAs grown at low temperatures *Thin solid films* **231.1–2** 61–73

[90] McIntosh K A, Nichols K B, Verghese S and Brown E R 1997 Investigation of ultrashort photocarrier relaxation times in low-temperature-grown GaAs *Appl. Phys. Lett.* **70** 354–6

[91] Stellmacher M, Nagle J, Lampin J F, Santoro P, Vaneecloo J and Alexandrou A 2000 Dependence of the carrier lifetime on acceptor concentration in GaAs grown at low-temperature under different growth and annealing conditions *J. Appl. Phys.* **88** 6026

[92] Loukakos P A, Kalpouzos C, Perakis I E, Hatzopoulos Z, Logaki M and Fotakis C 2001 Ultrafast electron trapping times in low-temperature-grown gallium arsenide: the effect of the arsenic precipitate spacing and size *Appl. Phys. Lett.* **79** 2883–5

[93] Tonouchi M, Kawasaki N, Yoshimura T, Wald H and Seidel P 2002 Pump and probe terahertz generation study of ultrafast carrier dynamics in low-temperature grown-GaAs *Japan. J. Appl. Phys.* **41** L706–L709

[94] Gregory I S, Tey C M, Cullis A G, Evans M J, Beere H E and Farrer I 2006 Two-trap model for carrier lifetime and resistivity behavior in partially annealed GaAs grown at low temperature *Phys. Rev.* B **73** 195201

[95] Moon K *et al* 2014 Generation and detection of terahertz waves using low-temperature-grown GaAs with an annealing process *ETRI J.* **36** 159–62

[96] Ma K, Urata R, Miller D A B and Harris J S 2004 Low-temperature growth of GaAs on Si used for ultrafast photoconductive switches *IEEE J. Quantum Electron.* **40** 800–4

[97] Yablonovitch E, Hwang D M, Gmitter T J, Florez L T and Harbison J P 1990 van der Waals bonding of GaAs epitaxial liftoff films onto arbitrary substrates *Appl. Phys. Lett.* **56** 2419–21

[98] Ríos R D V, Bikorimana S, Ummy M A, Dorsinville R and Seo S-W 2015 A bow-tie photoconductive antenna using a low-temperature-grown GaAs thin-film on a silicon substrate for terahertz wave generation and detection *J. Opt.* **17** 125802

[99] Heiliger H M, Vossebürger M, Roskos H G, Hey R, Ploog K and Kurz H 1996 THz signal generators based on lift-off LT-GaAs on transparent substrates *Seventh Int. Symp. Space Terahertz Technol. March 1996 Charlottesville* **1** 400

[100] Heiliger H-M, Vossebürger M, Roskos H G, Kurz H, Hey R and Ploog K 1996 Application of liftoff low-temperature-grown GaAs on transparent substrates for THz signal generation *Appl. Phys. Lett.* **69** 2903

[101] Awad M, Nagel M, Kurz H, Herfort J and Ploog K 2007 Characterization of low temperature GaAs antenna array terahertz emitters *Appl. Phys. Lett.* **91** 11–4

[102] Bacon D R *et al* 2016 Free-space terahertz radiation from a LT-GaAs-on-quartz large-area photoconductive emitter *Opt. Express* **24** 26986

[103] Yoneda H, Tokuyama K, Ueda K, Yamamoto H and Baba K 2001 High-power terahertz radiation emitter with a diamond photoconductive switch array *Appl. Opt.* **40** 6733

[104] Russell C, Wood C D, Burnett A D, Li L, Linfield E H, Davies A G and Cunningham J E 2013 Spectroscopy of polycrystalline materials using thinned-substrate planar Goubau line at cryogenic temperatures. *Lab Chip* **13** 4065–70

[105] Cunningham J, Wood C, Davies A G, Hunter I, Linfield E H and Beere H E 2005 Terahertz frequency range band-stop filters *Appl. Phys. Lett.* **86** 1–3

[106] Rios R D V, Bikorimana S, Dorsinville R and Seo S-W 2017 Terahertz-wave characterization of LTG-GaAs thin-film photoconductive antenna *IEEE J. Quantum Electron.* **23** 1–8

[107] Shi W, Hou L and Liu Z 2009 Terahertz generation from SI-GaAs stripline antenna with different structural parameters *J. Opt. Soc. Am.* B **26** 107–12

[108] Johnson M B, McGill T C and Paulter N G 1989 Carrier lifetimes in ion-damaged GaAs *Appl. Phys. Lett.* **54** 2424–6

[109] Lambsdorff M, Kuhl J, Rosenzweig J, Axmann A and Schneider J 1991 Subpicosecond carrier lifetimes in radiation-damaged GaAs *Appl. Phys. Lett.* **58** 1881–3

[110] Ganikhanov F, Lin G R, Chen W C, Chang C S and Pan C-L 1995 Subpicosecond carrier lifetimes in arsenic-ion-implanted GaAs *Appl. Phys. Lett.* **67** 3465

[111] Lin G R, Chen W C, Ganikhanov F, Chang C S and Pan C L 1996 Effect of rapid thermal annealing on carrier lifetime in arsenic-ion-implanted GaAs *Appl. Phys. Lett.* **69** 996

[112] Benicewicz P K, Roberts J P and Taylor A J 1994 Scaling of terahertz radiation from large-aperture biased photoconductors *J. Opt. Soc. Am.* B **11** 2533–46

[113] Liu T A *et al* 2005 Dark current and trailing-edge suppression in ultrafast photoconductive switches and terahertz spiral antennas fabricated on multienergy arsenic-ion-implanted GaAs *J. Appl. Phys.* **98** 013711

[114] Lloyd-Hughes J, Castro-Camus E, Fraser M D, Jagadish C and Johnston M B 2004 Carrier dynamics in ion-implanted GaAs studied by simulation and observation of terahertz emission *Phys. Rev.* B **70** 1–6

[115] Salem B, Morris D, Aimez V, Beauvais J and Houde D 2006 Improved characteristics of a terahertz set-up built with an emitter and a detector made on proton-bombarded GaAs photoconductive materials *Semicond. Sci. Technol.* **21** 283–6

[116] Salem B, Morris D, Salissou Y, Aimez V, Charlebois S, Chicoine M and Schiettekatte F 2006 Terahertz emission properties of arsenic and oxygen ion-implanted GaAs based photoconductive pulsed sources *J. Vac. Sci. Technol.* A **24** 774–7

[117] Winnerl S, Peter F, Nitsche S, Dreyhaupt A, Zimmermann B, Wagner M, Schneider H, Helm M and Kohler K 2008 Generation and detection of THz radiation with scalable antennas based on GaAs substrates with different carrier lifetimes *IEEE J. Sel. Top. Quantum Electron.* **14** 449–57

[118] Mangeney J 2012 THz photoconductive antennas made from ion-bombarded semiconductors *J. Infrared Millimeter Terahertz Waves* **33** 455–73

[119] Hönninger C *et al* 1999 ultrafast ytterbium-doped bulk lasers and laser amplifiers *Appl. Phys.* B **69** 3–17

[120] Wilke I, Dutta P S and Slobodtchikov E 2014 THz radiation emission from InPAs and GaInAs crystals 2014 39th International Conference on Infrared, Millimeter, and Terahertz waves (IRMMW-THz) *14–19 September 2014 (Tucson, AZ, USA)* **27** 2021

[121] Francoeur S, Seong M J, Mascarenhas A, Tixier S, Adamcyk M and Tiedje T 2003 Band gap of $GaAs_{1-x}Bi_x$, $0<x<3.6\%$ *Appl. Phys. Lett.* **82** 3874

[122] Bertulis K, Krotkus A, Aleksejenko G, Pačebutas V, Adomavičius R, Molis G and Marcinkevičius S 2006 GaBiAs: a material for optoelectronic terahertz devices *Appl. Phys. Lett.* **88** 201112

[123] Stanionytė S, Vailionis A, Bukauskas V, Tumėnas S, Bičiūnas A, Arlauskas A, Butkutė R and Krotkus A 2018

Thick epitaxial GaAsBi layers for terahertz components: the role of growth conditions *Lith. J. Phys.* **58** 126–34
[124] Kong M S, Kim J S, Han S P, Kim N, Moon K, Park K H and Jeon M Y 2016 Terahertz radiation using log-spiral-based low-temperature-grown InGaAs photoconductive antenna pumped by mode-locked Yb-doped fiber laser *Opt. Express* **24** 10095–100
[125] Hinkov I, Harzendorf G, Kluska S, Hinkov B, Kamaruzaman K and Beigang R 2007 Generation of terahertz pulsed radiation from photoconductive emitters using 1060 nm laser excitation 2007 Joint 32nd International Conference on Infrared and Millimeter Waves and the 15th International Conference on Terahertz Electronics *2–9 September 2007* (*Cardiff, UK*) 1–2
[126] Dietz R J B, Wilk R, Globisch B and Roehle H 2013 Low temperature grown Be-doped InGaAs/InAlAs photoconductive antennas excited at 1030 nm *J. Infrared Millimeter Terahertz Waves* **34** 231–7
[127] Dietz R J B, Brahm A, Velauthapillai A and Wilms A 2015 Low temperature grown photoconductive antennas for pulsed 1060 nm excitation: influence of excess energy on the electron relaxation *J. Infrared Millimeter Terahertz Waves* **36** 60–71
[128] Pacebutas V, Stanionyte S, Norkus R, Biciunas A, Urbanowicz A and Krotkus A 2019 Terahertz pulse emission from GaInAsBi *Appl. Phys. Lett.* **125** 174507
[129] Cheng K Y, Cho A Y, Christman S B, Pearsall T P and Rowe J E 1982 Measurement of the Γ-L separation in $Ga_{0.47}In_{0.53}As$ by ultraviolet photoemission *Appl. Phys. Lett.* **40** 4–7
[130] Fedorova K A, Gorodetsky A and Rafailov E U 2017 Compact all-quantum-dot-based tunable THz laser source *IEEE J. Sel. Top. Quantum Electron.* **23** 4
[131] Gorodetsky A, Yadav A, Avrutin E, Fedorova K A and Rafailov E U 2018 Photoelectric properties of InAs/GaAs quantum dot photoconductive antenna wafers *IEEE J. Quantum Electron.* **24** 2
[132] Gorodetsky A, Bazieva N and Rafailov E U 2019 Pump dependent carrier lifetimes in InAs/GaAs quantum dot photoconductive terahertz antenna structures *J. Appl. Phys.* **125** 1–6
[133] Gorodetsky A, Yadav A, Smirnov S V, Bazieva N and Rafailov E U 2020 Quantum dot photoconductive antenna-based compact setups for terahertz spectroscopy and imaging *Proceedings Volume 11499, Terahertz Emitters, Receivers, and Applications XI; 1149905 (2020)* **11499** 1–15
[134] Ludwig C and Kuhl J 1996 Studies of the temporal and spectral shape of terahertz pulses generated from photoconducting switches *Appl. Phys. Lett.* **69** 1194–6
[135] Fermann M E and Hartl I 2013 Ultrafast fibre lasers *Nat. Photon.* **7** 868–74
[136] Kondo T, Sakamoto M, Tonouchi M and Hangyo M 1999 Terahertz radiation from (111) InAs surface using 1.55 μm femtosecond laser pulses *Japan. J. Appl. Phys.* 2 **38** L 1035–L 1037
[137] Howells S C, Herrera S D and Schlie L A 1994 Infrared wavelength and temperature dependence of optically induced terahertz radiation from InSb *Appl. Phys. Lett.* **65** 2946–8
[138] Gu P, Tani M, Kono S, Sakai K and Zhang X C 2002 Study of terahertz radiation from InAs and InSb *J. Appl. Phys.* **91** 5533–7
[139] Ascázubi R, Shneider C, Wilke I, Pino R and Dutta P S 2005 Enhanced terahertz emission from impurity compensated GaSb *Phys. Rev.* B **72** 1–5
[140] Hatem O, Freeman J R, Cunningham J E, Cannard P J, Robertson M J, Linfield E H, Davies A G and Moodie D G 2016 Generation of terahertz radiation from Fe-doped InGaAsP Using 800 nm to 1550 nm pulsed laser excitation *J. Infrared Millimeter Terahertz Waves* **37** 415–25
[141] Urbanowicz A, Pačebutas V, Geižutis A, Stanionytė S and Krotkus A 2016 Terahertz time-domain-spectroscopy system based on 1. 55 μm fiber laser and photoconductive antennas from dilute bismides *AIP Adv.* **6** 2016
[142] Salas R, Guchhait S, Sifferman S D, McNicholas K M, Dasika V D, Krivoy E M, Jung D, Lee M L and Bank S R 2015 Growth and properties of rare-earth arsenide InGaAs nanocomposites for terahertz generation *Appl. Phys. Lett.* **106** 081103
[143] Globisch B, Dietz R J B, Kohlhaas R B, Göbel T, Schell M, Alcer D, Semtsiv M and Masselink W T 2017 Iron doped InGaAs: competitive THz emitters and detectors fabricated from the same photoconductor *J. Appl. Phys.* **121** 053102
[144] Singh A, Pashkin A, Winnerl S, Helm M and Schneider H 2018 Gapless broadband terahertz emission from a germanium photoconductive emitter *ACS Photonics* **5** 2718–23
[145] Schwagmann A, Zhao Z-Y, Ospald F, Lu H, Driscoll D C, Hanson M P, Gossard A C and Smet J H 2010 Terahertz emission characteristics of ErAs:InGaAs-based photoconductive antennas excited at 1.55 μm *Appl. Phys. Lett.* **96** 8–11
[146] Suzuki M and Tonouchi M 2005 Fe-implanted InGaAs terahertz emitters for 1.56 μm wavelength excitation *Appl. Phys. Lett.* **86** 1–3
[147] Gulwadi S M, Rao M V, Berry A K , Simons D S and Chi P H 1991 Transition metal implants in $In_{0.53}Ga_{0.47}As$ *Appl. Phys. Lett.* **69** 4222–7
[148] Mangeney J and Crozat P 2008 Ion-irradiated $In_{0.53}Ga_{0.47}As$ photoconductive antennas for THz generation and detection at 1.55 μm wavelength *C.R. Phys.* **9** 142–52
[149] Wood C D, Hatem O, Cunningham J E, Linfield E H, Davies A G, Cannard P J, Robertson M J and Moodie D G 2010 Terahertz emission from metal-organic chemical vapor deposition grown Fe:InGa Asusing 830 nm to 1.55 μm excitation *Appl. Phys. Lett.* **96** 98–101
[150] Mangeney J, Joulaud L, Crozat P, Lourtioz J M and Decobert J 2003 Ultrafast response (∼2.2 ps) of ion-irradiated InGaAs photoconductive switch at 1.55 μm *Appl. Phys. Lett.* **83** 5551–3
[151] Chimot N, Mangeney J, Joulaud L, Crozat P, Bernas H, Blary K and Lampin J F 2005 Terahertz radiation from heavy-ion-irradiated $In_{0.53}Ga_{0.47}As$ photoconductive antenna excited at 1.55 μm *Appl. Phys. Lett.* **87** 1–3
[152] Mangeney J, Chimot N, Meignien L, Zerounian N, Crozat P, Blary K, Lampin J F and Mounaix P 2007 Emission characteristics of ion-irradiated $In_{0.53}Ga_{0.47}As$ based photoconductive antennas excited at 1.55 μm *Opt. Express* **15** 8943
[153] Takazato A, Kamakura M, Matsui T, Kitagawa J and Kadoya Y 2007 Terahertz wave emission and detection using photoconductive antennas made on low-temperature-grown InGaAs with 1.56 μm pulse excitation *Appl. Phys. Lett.* **91** 2005–8
[154] Suzuki M, Tonouchi M, Fujii K I, Ohtake H and Hirosumi T 2006 Excitation wavelength dependence of terahertz emission from semiconductor surface *Appl. Phys. Lett.* **89** 1–4
[155] Sartorius B, Roehle H, Künzel H, Böttcher J, Schlak M, Stanze D, Venghaus H and Schell M 2008 All-fiber terahertz time-domain spectrometer operating at 1.5 μm telecom wavelengths *Opt. Express* **16** 9565
[156] Roehle H, Dietz R J B, Hensel H J, Böttcher J, Künzel H, Stanze D, Schell M and Sartorius B 2010 Next generation 1.5 μm terahertz antennas: mesa-structuring of InGaAs/InAlAs photoconductive layers *Opt. Express* **18** 2296–301

[157] Dietz R J B, Gerhard M, Stanze D, Koch M, Sartorius B and Schell M 2011 THz generation at 1.55 μm excitation: six-fold increase in THz conversion efficiency by separated photoconductive and trapping regions *Opt. Express* **19** 25911

[158] Mittendorff M, Xu M, Dietz R J B, Künzel H, Sartorius B, Schneider H, Helm M and Winnerl S 2013 Large area photoconductive terahertz emitter for 1.55 μm excitation based on an InGaAs heterostructure *Nanotechnology* **24** 21

[159] Zide J M, Wang Y and Jabbour C 2017 Materials for 1.55 m-pumped terahertz photoconductive switches: a review *Proceedings Volume 10383, Terahertz Emitters, Receivers, and Applications VIII; 103830N (2017)* (*San Diego, California, United States*) **10383**

[160] Kadow C, Jackson A W, Gossard A C, Bowers J E, Matsuura S and Blake A 2000 Self-assembled ErAs islands in GaAs for THz applications *Physica* E **7** 97–100

[161] Mingardi A, Zhang W-D, Brown E R, Feldman A D, Harvey T E and Mirin R P 2018 High power generation of THz from 1550-nm photoconductive emitters *Opt. Express* **26** 14472–8

[162] Poole I, Singer K E, Peaker A R and Wright A C 1992 Growth and structural characterization of molecular beam epitaxial erbium-doped GaAs *J. Cryst. Growth* **121** 121–31

[163] Driscoll D C, Hanson M P, Gossard A C and Brown E R 2005 Ultrafast photoresponse at 1.55 μm in InGaAs with embedded semimetallic ErAs nanoparticles *Appl. Phys. Lett.* **86** 1–3

[164] Williams K K, Taylor Z D, Suen J Y, Lu H, Singh R S, Gossard A C and Brown E R 2009 Toward a 1550 nm InGaAs photoconductive switch for terahertz generation *Opt. Lett.* **34** 3068–70

[165] Nandi U, Dutzi K, Deninger A, Lu H, Norman J, Gossard A C, Vieweg N and Preu S 2020 ErAs:In (Al) GaAs photoconductor-based time domain system with 4. 5 THz single shot bandwidth and emitted terahertz power of 164 μW *Opt. Lett.* **45** 2812–5

[166] Middendorf J R and Brown E R 2012 THz generation using extrinsic photoconductivity at 1550 nm *Opt. Express* **20** 16504–9

[167] Yukalov V I and Yukalova E P 2010 Dynamics of quantum dot superradiance *Phys. Rev.* B **81** 1–14

[168] Martin M and Brown E R 2015 Photoconductive materials for THz generation at 1550 nm: ErAs:GaAs vs InGaAs based materials *Terahertz, RF, Millimeter, Submillimeter-Wave Technol. Appl.* VIII (*San Francisco, California, United States*) **9362** 936207

[169] Madéo J, Margiolakis A, Zhao Z-Y, Hale P J, Man M K L, Zhao Q-Z, Peng W, Shi W-Z and Dani K M 2015 Ultrafast properties of femtosecond-laser-ablated GaAs and its application to terahertz optoelectronics *Opt. Lett.* **40** 3388

[170] Collier C M, Stirling T J, Hristovski I R, Krupa J D A and Holzman J F 2016 Photoconductive terahertz generation from textured semiconductor materials *Sci. Rep.* **6** 23185

[171] Kono S, Tani M and Sakai K 2002 Coherent detection of mid-infrared radiation up to 60 THz with an LT-GaAs photoconductive antenna *IEEE Proc. Optoelectron.* **149** 1–5

[172] Cai Y, Brener I, Lopata J, Wynn J, Pfeiffer L and Federici J 1997 Design and performance of singular electric field terahertz photoconducting antennas *Appl. Phys. Lett.* **71** 2076–8

[173] Dreyhaupt A, Winnerl S, Dekorsy T and Helm M 2005 High-intensity terahertz radiation from a microstructured large-area photoconductor *Appl. Phys. Lett.* **86** 1–3

[174] Matthäus G, Nolte S, Hohmuth R, Voitsch M, Richter W, Pradarutti B, Riehemann S, Notni G and Tünnermann A 2008 Microlens coupled interdigital photoconductive switch *Appl. Phys. Lett.* **93** 091110

[175] Berry C W, Wang N, Hashemi M R, Unlu M and Jarrahi M 2013 Significant performance enhancement in photoconductive terahertz optoelectronics by incorporating plasmonic contact electrodes *Nat. Commun.* **4** 1622

[176] Yang S H, Hashemi M R, Berry C W and Jarrahi M 2014 7.5% optical-to-terahertz conversion efficiency offered by photoconductive emitters with three-dimensional plasmonic contact electrodes *IEEE Trans. Terahertz Sci. Technol.* **4** 575–81

[177] Yardimci N T, Yang S H, Berry C W and Jarrahi M 2015 High-power terahertz generation using large-area plasmonic photoconductive emitters *IEEE Trans. Terahertz Sci. Technol.* **5** 223–9

[178] You D, Dykaar D R, Jones R R and Bucksbaum P H 1993 Generation of high-power sub-single-cycle 500-fs electromagnetic pulses *Opt. Lett.* **18** 290

[179] Budiarto E, Margolies J, Jeong S, Son J, Bokor J and Member S 1996 High-intensity terahertz pulses at 1-kHz repetition rate *IEEE J. Quantum Electron.* **32.10** 1839–46

[180] Darrow J T, Zhang X C, Auston D H and Morse J D 1992 Saturation properties of large-aperture photoconducting antennas *IEEE J. Quantum Electron.* **28** 1607–16

[181] Kim D S and Citrin D S 2006 Coulomb and radiation screening in photoconductive terahertz sources *Appl. Phys. Lett.* **88** 161117

[182] Kono S, Tani M and Sakai K 2001 Ultrabroadband photoconductive detection: comparison with free-space electro-optic sampling *Appl. Phys. Lett.* **79** 898–900

[183] Vieweg N, Mikulics M, Scheller M, Ezdi K, Wilk R, Hübers H W and Koch M 2008 Impact of the contact metallization on the performance of photoconductive THz antennas *Opt. Express* **16** 19695

[184] Shi W, Hou L and Wang X 2011 High effective terahertz radiation from semi-insulating-GaAs photoconductive antennas with ohmic contact electrodes *J. Appl. Phys.* **110** 023111

[185] Singh A, Welsch M, Winnerl S, Helm M and Schneider H 2019 Improved electrode design for interdigitated large-area photoconductive terahertz emitters *Opt. Express* **27** 13108

[186] Singh A, Winnerl S, König-Otto J C, Stephan D R, Helm M and Schneider H 2016 Plasmonic efficiency enhancement at the anode of strip line photoconductive terahertz emitters *Opt. Express* **24** 22628–34

[187] Matthäus G, Nolte S, Hohmuth R, Voitsch M, Richter W, Pradarutti B, Riehemann S, Notni G and Tünnermann A 2009 Large-area microlens emitters for powerful THz emission *Appl. Phys.* B **96** 233–5

[188] Garufo A *et al* 2019 A connected array of coherent photoconductive pulsed sources to generate mW average power in the submillimeter wavelength band *IEEE Trans. Terahertz Sci. Technol.* **9** 221–36

[189] Berry C W, Hashemi M R and Jarrahi M 2014 Generation of high power pulsed terahertz radiation using a plasmonic photoconductive emitter array with logarithmic spiral antennas *Appl. Phys. Lett.* **104** 081122

[190] Pradarutti B, Müller R, Freese W, Matthäus G, Riehemann S, Notni G, Nolte S and Tünnermann A 2008 Terahertz line detection by a microlens array coupled photoconductive antenna array *Opt. Express* **16** 18443–50

[191] Maussang K, Brewer A, Palomo J, Manceau J-M, Colombelli R, Sagnes I, Mangeney J, Tignon J and Dhillon S S 2016 Echo-less photoconductive antenna sources for high-resolution terahertz time-domain spectroscopy *IEEE Trans. Terahertz Sci. Technol.* **2016-Novem** 20–5

[192] Beck M, Schäfer H, Klatt G, Demsar J, Winnerl S, Helm M and Dekorsy T 2010 Impulsive terahertz radiation with high electric fields from an amplifier-driven large-area photoconductive antenna *Opt. Express* **18** 9251

[193] Shen Y C, Upadhya P C, Linfield E H, Beere H E and Davies A G 2003 Ultrabroadband terahertz radiation from low-temperature-grown GaAs photoconductive emitters *Appl. Phys. Lett.* **83** 3117–9

[194] Madéo J, Jukam N, Oustinov D, Rosticher M, Rungsawang R, Tignon J and Dhillon S S 2010 Frequency tunable terahertz interdigitated photoconductive antennas *Electron. Lett.* **46** 611–3

[195] Tani M, Hirota Y, Que C T, Tanaka S, Hattori R, Yamaguchi M, Nishizawa S and Hangyo M 2006 Novel terahertz photoconductive antennas *Int. J. Infrared Millimeter Waves* **27** 531–46

[196] Winnerl S, Zimmermann B, Peter F, Schneider H and Helm M 2009 Terahertz Bessel−Gauss beams of radial and azimuthal polarization from microstructured photoconductive antennas *Opt. Express* **17** 1571

[197] Jeon T I, Zhang J and Grischkowsky D 2005 THz Sommerfeld wave propagation on a single metal wire *Appl. Phys. Lett.* **86** 1–3

[198] Park S, Jin K and Jeong K H 2011 Nanoplasmonic photoconductive antenna for high power terahertz emission *16th Int. Solid-State Sensors, Actuators Microsystems Conf. IEEE* pp W3P.132

[199] Park S G, Jin K H, Yi M, Ye J C, Ahn J and Jeong K H 2012 Enhancement of terahertz pulse emission by optical nanoantenna *ACS Nano* **6** 2026–31

[200] Berry C W and Jarrahi M 2012 Terahertz generation using plasmonic photoconductive gratings *New J. Phys.* **14** 105029

[201] Yardimci N T and Jarrahi M 2015 3.8 mW terahertz radiation generation through plasmonic nano-antenna arrays *2015 IEEE International Symposium on Antennas and Propagation & USNC/URSI National Radio Science Meeting 19–24 July 2015* (*Vancouver, BC, Canada*) pp 2113–34

[202] Lepeshov S, Gorodetsky A, Krasnok A, Toropov N, Vartanyan T A, Belov P, Alú A and Rafailov E U 2018 Boosting terahertz photoconductive antenna performance with optimised plasmonic nanostructures *Sci. Rep.* **8** 1–7

[203] Dionne J A, Sweatlock L A, Atwater H A and Polman A 2005 Planar metal plasmon waveguides: frequency-dependent dispersion, propagation, localization, and loss beyond the free electron model *Phys. Rev.* B **72** 1–11

[204] Moon K, Lee I-M, Shin J-H, Lee E S, Kim N, Lee W-H, Ko H, Han S-P and Park K H 2015 Bias field tailored plasmonic nano-electrode for high-power terahertz photonic devices *Sci. Rep.* **5** 1–9

[205] Jooshesh A, Bahrami-Yekta V, Zhang J, Tiedje T, Darcie T E and Gordon R 2015 Plasmon-enhanced below bandgap photoconductive terahertz generation and detection *Nano Lett.* **15** 8306–10

[206] Yardimci N T, Lu H and Jarrahi M 2016 High power telecommunication-compatible photoconductive terahertz emitters based on plasmonic nano-antenna arrays *Appl. Phys. Lett.* **109** 1–5

[207] Yardimci N T, Salas R, Krivoy E M, Nair H P, Bank S R and Jarrahi M 2015 Impact of substrate characteristics on performance of large area plasmonic photoconductive emitters *Opt. Express* **23** 32035

[208] Lepeshov S, Gorodetsky A, Krasnok A, Rafailov E and Belov P 2017 Enhancement of terahertz photoconductive antenna operation by optical nanoantennas *Laser Photonics Rev.* **11** 1–21

[209] Yardimci N T and Jarrahi M 2018 Nanostructure-enhanced photoconductive terahertz emission and detection *Nano. Micro. Small* **1802437** 1–14

[210] Darrow J T, Zhang X C and Auston D H 1991 Power scaling of large-aperture photoconducting antennas *Appl. Phys. Lett.* **58** 25–7

[211] Jones R R, You D and Bucksbaum P H 1993 Ionization of Rydberg atoms by subpicosecond half-cycle electromagnetic pulses *Phys. Rev. Lett.* **70** 1236–9

[212] Cook D J, Chen J X, Morlino E A and Hochstrasser R M 1999 Terahertz-field-induced second-harmonic generation measurements of liquid dynamics *Chem. Phys. Lett.* **309** 221–8

[213] Ropagnol X, Morandotti R, Ozaki T and Reid M 2011 Toward high-power terahertz emitters using large aperture ZnSe photoconductive antennas *IEEE Photon. J.* **3** 174–86

[214] Siebert K J, Lisauskas A, Löffler T and Roskos H G 2004 Field screening in low-temperature-grown GaAs photoconductive antennas *Japan. J. Appl. Phys.* 1 **43** 1038–43

[215] Hattori T, Egawa K, Ookuma S I and Itatani T 2006 Intense terahertz pulses from large-aperture antenna with interdigitated electrodes *Japan. J. Appl. Phys.* 2 **45** 4L

[216] Upadhya P C, Fan W, Burnett A, Cunningham J, Davies A G, Linfield E H, Lloyd-Hughes J, Castro-Camus E, Johnston M B and Beere H 2007 Excitation-density-dependent generation of broadband terahertz radiation in an asymmetrically excited photoconductive antenna *Opt. Lett.* **32** 2297–9

[217] Ralph S E and Grischkowsky D 1991 Trap-enhanced electric fields in semi-insulators: the role of electrical and optical carrier injection *Appl. Phys. Lett.* **59** 1972–5

[218] Holzman J F and Elezzabi A Y 2003 Two-photon photoconductive terahertz generation in ZnSe *Appl. Phys. Lett.* **83** 2967–9

[219] Ropagnol X, Bouvier M, Cote C Y, Reid M, Gauthier M A and Ozaki T 2015 Generation of elliptically polarized half-cycle terahertz pulses generated by 6H-SiC large aperture photoconductive antenna *2015 Conference on Lasers and Electro-Optics (CLEO) 10–15 May 2015* (*San Jose, CA, USA*) pp SM2H.4

[220] Ropagnol X, Bouvier M, Reid M and Ozaki T 2014 Improvement in thermal barriers to intense terahertz generation from photoconductive antennas *J. Appl. Phys.* **116** 043107

[221] Elezzabi A Y, Houtman H and Meyer J 1994 Time-resolved impact ionization in ZnSe high-voltage switches *IEEE Trans. Plasma Sci.* **22** 1043–8

[222] Ropagnol X, Blanchard F, Ozaki T and Reid M 2013 Intense terahertz generation at low frequencies using an interdigitated ZnSe large aperture photoconductive antenna *Cit. Appl. Phys. Lett.* **103** 161108

[223] Ropagnol X, Chai X, Raeis-Zadeh S M, Safavi-Naeini S, Kirouac-Turmel M, Bouvier M, Cote C-Y, Reid M, Gauthier M A and Ozaki T 2017 Influence of gap size on intense THz generation from ZnSe interdigitated large aperture photoconductive antennas *IEEE J. Sel. Top. Quantum Electron.* **23** 1–8

[224] Ropagnol X, Kovács Z, Gilicze B, Zhuldybina M, Blanchard F, Garcia-Rosas C M, Szatmári S, Földes I B and Ozaki T 2019 Intense sub-terahertz radiation from wide-bandgap semiconductor based large-aperture photoconductive antennas pumped by UV lasers *New J. Phys.* **21** 113042

[225] Wang F *et al* 2017 Short terahertz pulse generation from a dispersion compensated modelocked semiconductor laser *Laser Photonics Rev.* **11** 1700013

[226] Maysonnave J *et al* 2012 Mode-locking of a terahertz laser by direct phase synchronization *Opt. Express* **20** 20855–62
[227] Bachmann D *et al* 2016 Pulse generation and spectral optimization of broadband terahertz quantum cascade lasers *2016 41st International Conference on Infrared, Millimeter, and Terahertz waves (IRMMW-THz) 25–30 September 2016* (*Copenhagen, Denmark*) pp 18–25
[228] Lee Y S, Meade T, Norris T B and Galvanauskas A 2001 Tunable narrow-band terahertz generation from periodically poled lithium niobate *Appl. Phys. Lett.* **78** 3583–5
[229] Dey I *et al* 2017 Highly efficient broadband terahertz generation from ultrashort laser filamentation in liquids *Nat. Commun.* **8** 1184
[230] Wu X *et al* 2018 Highly efficient generation of 0.2 mJ terahertz pulses in lithium niobate at room temperature with sub-50 fs chirped Ti:sapphirelaser pulses *Opt. Express* **26** 7107
[231] Saraceno C J 2018 Mode-locked thin-disk lasers and their potential application for high-power terahertz generation *J. Opt.* **20** 044010